Global Precipitation Efficiency from a Satellite Perspective

Megan Schaaf

Atmospheric and Oceanic Sciences

University of Wisconsin - Madison

December 18, 2025

Abstract

Convective clouds are fundamental to Earth's climate system, influencing both the global water cycle and planetary radiation budget. However, the processes controlling precipitation efficiency (PE) remain poorly represented in weather models. Because PE links cloud microphysics, storm dynamics, and large-scale radiative feedbacks, understanding its variability across environments is essential. This study examines PE in six regions of intense convection across the tropics and mid-latitudes, using coincident CloudSat and GPM observations combined with an A-Train based Convective Object Database. Key hydrometeor properties, including ice water path, liquid water path, and surface rain rate, are analyzed to quantify PE globally. Results show that PE varies systematically with storm type, environment, and large-scale dynamics, revealing more complexity than simple latitudinal distinctions. While tropical and midlatitude storms differ in cloud structure and hydrometeor loading, these alone do not explain PE variability. Metrics of convective vertical structure, such as relative center of gravity (rCoG), and local shear emerge as key predictors, highlighting the importance of dynamical support and storm maturity. PE also correlates with cloud radiative properties, suggesting that the balance between anvil formation and surface-reaching precipitation is influenced by microphysics affecting both radiative forcing and column water budgets. Comparisons across phases of the Walker circulation indicate that large-scale vertical motion can outweigh latitude in controlling PE. Overall, PE reflects an interplay of mesoscale dynamics, microphysical structure, and global circulations, emphasizing the need to consider lifecycle and environmental context in interpreting convective precipitation efficiency.

Contents

1 Introduction

The role of deep convection in Earth's radiation budget, especially in the tropics, has long been central to climate science. Since the Earth Radiation Budget Experiment (ERBE) launched in 1984, it has been understood that Earth's radiative balance is maintained through heat redistribution with net cooling at the poles and net warming at the equator. Because clouds mediate much of this balance, their response to climate change may significantly alter radiative forcing patterns. Recent studies emphasize not only net radiation changes but also the importance of cloud-top temperature and cloud optical properties in shaping radiative effects (Hu and Stamnes 2000; L'Ecuyer et al. 2019). High, optically thick clouds, particularly those produced by deep convection, contribute disproportionately to net cooling, accounting for up to 25 percent of global net cloud radiative forcing (Hartmann 1992). However, the magnitude and even sign of future cloud feedbacks remain uncertain due to challenges in representing convection and cloud microphysics in models.

Understanding the dynamics and microphysics of global convection is particularly important in the context of a warming climate. As global temperatures rise, the frequency, intensity, and vertical structure of deep convective systems are expected to change, potentially altering both precipitation efficiency (PE), which is broadly how efficiently condensate turns into precipitation, and cloud radiative effects (Stephens et al. 2010; L'Ecuyer et al. 2019). Enhanced upper-tropospheric humidity and increased ice cloud formation may shift the net cloud radiative effect toward more positive feedbacks, reinforcing warming in the tropics. Various changes in convection and PE could also modify the partitioning of precipitation between stratiform and convective components, influencing the distribution and magnitude of rainfall at the surface. The full importance and influence of PE in deep convection will be elaborated more below.

From a societal perspective, improved understanding of these processes is critical for enhancing precipitation forecasts, managing freshwater resources, and anticipating climate impacts on tropical regions that are highly sensitive to changes in rainfall patterns (Chadwick et al. 2016). Small-scale microphysical processes, such as secondary ice production, droplet freezing, and entrainment, can therefore have large-scale implications for the atmospheric energy balance, water cycle, and regional hydrology. Integrating knowledge of convective microphysics, precipitation efficiency, and radiative effects is essential not only for advancing

climate modeling but also for practical applications in water resource management and disaster preparedness.

In addition to their radiative influence, deep convective clouds also play a pivotal role in Earth's hydrological cycle, where PE becomes a key metric linking cloud microphysics to surface rainfall. For the purposes of this reasearch, PE refers to the fraction of condensed water in a cloud that ultimately falls as precipitation, rather than remaining suspended, evaporating, or being transported elsewhere within the system. It should be noted that outside of this study, PE is more generally defined as the ratio of rainfall to water vapor entrained into the storm, primarly in the modeling community (Sui et al. 2020; Smalley and Rapp 2021). Our definition was adapted from this in order to incorporate observable quantities, whereas variables used in models such as water vapor convergence are not feasible to retrieve from a remote sensing perspective. This efficiency is shaped by factors such as environmental humidity, storm dynamics, and microphysical processes like riming, aggregation, and melting. Importantly, PE is not only a measure of rainfall output but also a proxy for how much latent heat is released into the atmosphere during phase changes, which feeds back into atmospheric circulation and stability (Sui et al. 2020). Systems with low PE may produce large amounts of cloud ice and extensive anvils that significantly affect top-of-atmosphere radiation, but contribute less to surface rainfall. Conversely, high-PE systems have a more direct hydrological impact. Understanding PE is therefore essential not only for improving precipitation forecasts but also for interpreting how convective clouds influence both radiative forcing and global water and energy cycles.

Although the precipitating portion of a convective system typically occupies only a small fraction of the total cloud area (Kukulies et al. 2022), these convective events are responsible for delivering a large share of rainfall (Roca and Fiolleau 2020), particularly in the tropics, where deep convection dominates the precipitation budget. This disparity between cloud area and rainfall emphasizes the importance of PE as a critical link between cloud microphysics and the surface water budget. In regions where deep convection is frequent, such as the tropical oceans or continental monsoon zones (Aumann and Ruzmaikin 2013), variations in PE directly influence water availability, soil moisture, runoff, and freshwater resources. Maritime systems, which often exhibit higher PE due to efficient warm-rain processes (Matsui et al. 2016), can contribute more effectively to steady rainfall, whereas continental storms, despite their intensity, may show lower PE due to strong updrafts and abundant ice-phase processes that recycle condensate into ice and/or vapor and limit surface rainfall.

On a global scale, the cumulative effect of convective precipitation, even from relatively small precipitating regions, plays a major role in maintaining the energy and moisture balance of the atmosphere (Dagan and Stier et al. 2020; Pendergass and Hartmann 2014). Current research on PE spans both observational and modeling approaches, each offering complementary insights yet presenting notable limitations. Observational studies provide invaluable real-world evidence of PE under diverse environmental and climatic conditions, capturing the complexity of atmospheric processes and regional variability (Frankhauser 1988; Mohd Anip and Market 2006; Narsey et al. 2019; Zhao et al. 2024). However, such studies are often geographically constrained and limited in their capacity to generalize PE behavior globally. Modeling studies, on the other hand, allow controlled experimentation on the sensitivity of PE to factors such as microphysical schemes, humidity, and updraft intensity, illuminating the underlying mechanisms that govern precipitation outcomes (Sui et al. 2020; Huo et al. 2024; Jo et al. 2025).

Despite these advantages, models continue to exhibit substantial uncertainty in estimating PE, largely due to persistent errors in the representation of rain rate, condensate loading, and cloud microphysics (Blossey et al. 2007; Varble et al. 2014; Satoh et al. 2019). Despite extensive observational and modeling studies of precipitation efficiency, significant gaps remain in our understanding of how PE varies globally, particularly in regions where in situ measurements are sparse and model uncertainties are high. Most observational studies are regionally focused, capturing PE under specific environmental conditions, while global models often struggle to accurately represent cloud microphysics and convective dynamics, leading to persistent biases in PE estimation (Blossey et al. 2007; Varble et al. 2014). To address this critical gap, the present research aims to evaluate precipitation efficiency on a global scale using satellite-based remote sensing. By leveraging comprehensive, high-resolution satellite datasets, this study seeks to bridge the divide between localized observations and global modeling efforts, providing a more robust understanding of the processes that govern PE and their implications for the hydrological cycle and climate feedbacks.

1.1 Precipitation Efficiency

A key factor in determining both the radiative properties and the PE of convective clouds is the role of ice microphysics. The processes that govern the formation, growth, and distribution of ice particles within deep convective systems exert strong control over how much water ultimately falls as precipitation, and how the

cloud interacts with radiation in both the shortwave and longwave spectra. Ice microphysics encompasses a range of processes, including nucleation, deposition, riming, aggregation, and melting, through which various ice-phase hydrometeors, such as ice crystals, snowflakes, graupel, and hail, form and evolve in cloud systems. These processes determine the vertical and horizontal structure of frozen hydrometeors in the upper and mid-levels of convective clouds, which in turn impacts both precipitation generation and cloud optical properties.

Radiatively, ice microphysics profoundly shapes a convective cloud's top-of-atmosphere energy signature. High, ice-rich anvils composed of non-precipitating ice crystals can significantly reduce outgoing longwave radiation (OLR) by emitting at cold temperatures near the tropical tropopause (Hartmann and Berry 2017). The optical thickness, particle size, and vertical extent of ice clouds control their emissivity and reflectivity, thereby influencing both longwave warming (by trapping heat below) and shortwave cooling (by reflecting incoming solar radiation) (Hong et al. 2009; Yi 2022). Variability in ice content and distribution, such as the presence of detrained anvil cirrus versus active convective cores, can thus lead to substantial differences in the net cloud radiative effect (CRE) (Hartmann and Berry 2017).

Ice microphysics serves as a critical bridge between the dynamics of convection, precipitation formation, and cloud-radiation interactions. Understanding and accurately representing these processes is essential for predicting both local hydrological impacts and global climate feedbacks, particularly in the tropics where deep convection dominates the vertical transport of water and energy (Schiro and Neelin 2019).

1.1.1 Ice Water Path

The ice water path (IWP) is ultimately determined by the moisture available for freezing, and cirrus anvil clouds tend to coincide with regions of high free-tropospheric relative humidity. The geophysical significance of high ice water content (HIWC) environments in tropical mesoscale convective systems (MCSs) has yet to be fully understood. However, it is generally accepted that ice initiation mechanisms within the convective cores of tropical MCSs are closely linked to the formation and longevity of anvil cirrus. The relevance of this to updraft dynamics is highlighted by Korolev et al. (2024), which found that nearly all convective regions with vertical velocities greater than 2 m s^{-1} were associated with enhanced ice water content (IWC). HIWC regions were observed to extend around convective updrafts over horizontal scales ranging from a

few hundred meters to several tens of kilometers. Areas of elevated IWC correlate with strong convective cores characterized by high radar reflectivities and intense updraft velocities (Korolev et al. 2024). Although this relationship was not observed in all cases, the authors note that their aircraft-based sampling strategy may have led to instances of HIWC without concurrent updrafts, as convection may have weakened by the time measurements were taken. Importantly, Korolev et al. (2024) also report that the majority of secondary ice production (SIP) regions were co-located with convective updrafts, indicating that updrafts enhance ice concentrations not only through heterogeneous and homogeneous nucleation, but also through ice multiplication processes. SIP generates additional ice particles from pre-existing ice, especially in mixed-phase convective clouds with strong updrafts. By increasing ice concentrations beyond primary nucleation, SIP enhances precipitation formation and influences PE, making it a critical process for understanding cloud microphysics and rainfall outcomes (Zhao and Liu 2022).

Updrafts play a critical role in initiating new hydrometeor formation by lofting liquid droplets and ice nuclei into colder atmospheric layers. Vertical velocity has been shown to increase the median values of both IWC and liquid water content (LWC) with height, as updrafts transport high concentrations of small particles upward (Heymsfield et al., 2009). This suggests that strong vertical motion promotes additional droplet activation and subsequent freezing, leading to higher ice particle concentrations aloft. While enhanced ice production might initially imply greater potential for precipitation, we anticipate it may reduce precipitation efficiency. Increased ice particle concentrations, particularly those resulting from SIP, can generate numerous small particles that remain suspended for extended periods. Luke et al. (2021) observed that regions of intense updrafts strongly coincide with zones of active SIP, likely due to updraft-enhanced freezing fragmentation, in which colliding ice particles shatter to form new ice crystals. Although Luke et al. (2021) focused on mixed-phase Arctic clouds, similar mechanisms have been identified in tropical deep convection. Huang et al. (2022) found that total ice particle production rates in strong updraft regions of tropical convection were approximately four times higher than in weaker regions, confirming that updraft-enhanced fragmentation is a dominant process. We believe this resulting abundance of small ice particles aloft can decrease PE by storing condensate as suspended ice, particularly within anvils, and by promoting sublimation as particles fall through drier layers. Furthermore, competition among numerous small crystals for limited water vapor, especially under high supersaturation, can suppress individual growth rates. Under

moderate updrafts ($\sim$4 m s^{-1}), diffusional growth can exceed the available vapor supply, leading to droplet evaporation and a depletion of liquid water.

In strong convective systems, particularly in the tropics, vigorous updrafts can loft substantial amounts of water vapor and condensate into the upper troposphere. At these altitudes, where temperatures are well below freezing, much of the condensate exists as ice particles such as snow, graupel, and aggregates (Zipser, 2003; Houze, 2004). These particles often remain suspended for extended periods within the widespread anvil clouds and upper-level outflows that form as detrainment occurs from convective cores (Yuan and Houze, 2010). This lofted ice reduces PE because water is retained aloft longer and is less likely to reach the surface as precipitation. In anvil regions, ice particles can be advected far from their source and may never grow large enough to fall as rain. Instead, they frequently sublimate into vapor as they descend into drier atmospheric layers, effectively removing condensate from the precipitation column. This process results in a net loss of condensate from the surface hydrological cycle and underscores the role of both microphysical and dynamical processes in controlling precipitation efficiency. Thus, while deep convection is highly effective at producing condensate, the combination of strong updrafts, prolonged suspension times, and sublimation in outflow regions can significantly suppress the efficiency with which condensate is converted into rainfall.

Another key microphysical control on PE is the size and habit of ice particles within convective clouds. Larger particles, such as graupel or snow aggregates, have higher terminal velocities, which increase the likelihood that they will descend rapidly enough to reach the surface before sublimating or melting. This enhances PE by ensuring that a greater fraction of condensed water contributes directly to surface precipitation. In contrast, small ice crystals or pristine snowflakes fall much more slowly and can remain suspended for long periods, particularly in regions of strong updrafts or subsaturated air. We anticipate that this extended residence time increases the probability of sublimation before melting, thereby reducing PE. The vertical structure of humidity and temperature also plays a crucial role. In dry layers below cloud base, slow falling particles are especially susceptible to sublimation. Consequently, cloud systems dominated by small ice particles and high-altitude, non-precipitating anvil clouds tend to exhibit low PE, even though they are radiatively significant. The size distribution and fall behavior of ice hydrometeors therefore represent fundamental determinants of how efficiently a cloud can convert condensed moisture into measurable precipitation at the surface.

1.1.2 Liquid Water Path

The behavior of liquid water within convective clouds is tightly controlled by the interplay between microphysical growth processes and vertical air motion. Accretional growth, where liquid droplets collide and coalesce with ice or other hydrometeors, serves as a key pathway for the formation of condensate. However, this process also rapidly depletes the local liquid water content (LWC), particularly in environments with strong vertical velocities (Heymsfield et al., 2009). As updraft strength increases, the residence time of supercooled liquid droplets within mixed-phase regions becomes shorter, and the transition from liquid to ice occurs more efficiently due to enhanced freezing and riming processes. In such regimes, LWC is often quickly converted into ice, reducing the overall availability of liquid condensate for warm-rain processes. Observations by Korolev et al. (2024) indicate that in convective regions with vertical velocities exceeding 2 m s^{-1}, liquid water was nearly absent, suggesting a strongly glaciated environment dominated by ice-phase microphysics.

The rapid depletion of LWC under strong updraft conditions has several implications for PE. In weak to moderate updrafts, sustained LWC supports collision–coalescence processes that enhance the efficiency of rainfall formation, especially in maritime environments where warm rain production dominates. Conversely, in vigorous convective systems, liquid droplets are lofted above the freezing level before they can effectively coalesce, promoting glaciation instead of direct rain formation (Rosenfeld and Lensky, 1998). This transition marks a shift from warm-rain dominated precipitation to mixed-phase or ice-dominated regimes, which are typically associated with lower PE due to increased hydrometeor recycling and sublimation losses. Furthermore, the depletion of LWC by riming and freezing not only alters microphysical growth pathways but also influences radiative properties, as liquid-rich clouds have higher optical depths and reflectivity compared to their glaciated counterparts (Yi et al. 2017). Thus, variations in LWC driven by updraft intensity and accretional processes play a central role in determining both the radiative and hydrological impacts of convective systems.

In the tropical atmosphere, high stratiform clouds contribute substantially to upper-tropospheric humidity, with their formation and characteristics largely determined by the microphysics and dynamics of convective cores (Sun and Lindzen 1993). Entrainment, particularly in the first few kilometers above cloud

base, contributes to the dilution of tropical convection (Zipser 2003), though the degree of entrainment remains debated (Heymsfield et al. 2010). While these uncertainties affect cloud droplet and ice particle activation, for the purposes of this study, the focus remains on broader impacts of microphysical processes on precipitation efficiency (PE). Warm-cloud processes in tropical convection, combined with very moist vertical profiles, often support higher PE, as ice melting occurs with minimal evaporation, efficiently transferring condensate to the surface.

In summary, strong convective updrafts, while highly effective at generating condensate, particularly in the form of ice, can paradoxically suppress precipitation efficiency. By enhancing glaciation and promoting secondary ice production, vigorous vertical motions shift microphysical growth pathways toward regimes dominated by numerous small, slowly falling particles with extended residence times aloft. These particles are more prone to sublimation and evaporation during their descent, effectively removing condensate from the precipitation column before it reaches the surface. Consequently, even though deep convective systems with strong updrafts produce abundant condensate, much of it can be retained or lost within the cloud system rather than contributing to surface rainfall, leading to an anticipated reduced overall precipitation efficiency.

1.2 Radiative Implications

A number of processes operate across microphysical and synoptic scales to govern the radiative impacts of clouds, particularly in the tropics. While the net cloud radiative forcing in the tropics has often been found to be close to zero (Xu et al. 2025), certain large-scale conditions, such as strong ocean heat transport or pronounced land-sea thermal contrasts, can shift the balance, yielding a significantly negative forcing in convective regions (Hartmann et al. 2001). The near-neutral net cloud radiative effect (NCRE) of tropical convective systems reflects a cancellation between the strong shortwave cooling of deep, rainy convective cores and the compensating longwave warming of thinner cirrus outflows. Although often described as "neutral," this balance may change in a warming climate, with potentially important feedbacks (Hartmann et al. 2018). For instance, a warmer and moister upper troposphere may promote enhanced ice cloud formation and longer-lived anvils, resulting in a more positive NCRE that reinforces surface warming. Satellite missions such as CloudSat and CALIPSO, which are discussed further in Section 2, have provided unprecedented vertical

profiles of cloud structure and radiative properties, revealing the complex layering of convective systems and the distinct radiative contributions from precipitating cores and their associated cirrus shields.

1.2.1 Growth Mechanisms

The growth pathways of ice particles within deep convective clouds have direct implications for atmospheric radiation, especially in the tropics where such systems are prevalent. As updrafts intensify, they enhance ice nucleation, secondary ice production, and diffusional growth, leading to dense populations of small ice crystals aloft, particularly in the upper troposphere and anvil outflows (Heymsfield et al. 2009; Huang et al. 2022). These ice particles strongly modulate both shortwave and longwave radiation. Small crystals in thick anvils are highly reflective to incoming solar radiation, increasing cloud albedo and producing a net shortwave cooling effect at the top of the atmosphere (Hartmann et al. 2001). Simultaneously, these same particles are efficient absorbers and emitters of longwave radiation due to their high altitude and low temperature, producing a greenhouse effect that traps outgoing infrared radiation.

The balance between these competing radiative effects depends on the size, shape, concentration, and vertical distribution of ice particles: all regulated by the strength and structure of updrafts. Strong updrafts favor rapid glaciation and extensive anvil formation, enhancing both longwave warming and shortwave cooling. Thin cirrus formed by detrainment of small crystals tends to warm the atmosphere, while thicker anvils dominated by larger crystals yield a net cooling effect (Wolf et al. 2023). The long residence times of ice aloft extend the cloud's radiative influence beyond the convective core's lifetime. Thus, the same microphysical processes that control precipitation efficiency also determine the optical thickness and radiative forcing of anvils, linking cloud dynamics, hydrology, and energy balance in a unified framework. Accurately representing these coupled processes in global climate models remains a central challenge for predicting Earth's energy balance and climate sensitivity (Wang et al. 2025; Bock and Lauer 2024).

1.2.2 Iris Effect

The "iris effect" is a hypothesized negative climate feedback mechanism involving tropical high clouds and their influence on Earth's radiation budget (Lindzen et al. 2001). It suggests that as tropical sea surface temperatures (SSTs) rise, the area covered by high-level cirrus clouds decreases, allowing more infrared

radiation to escape to space and thereby cooling the planet. While some studies have found evidence consistent with this mechanism, others report little to no support, or even positive feedbacks in similar regions (Lin et al. 2002; Hartmann and Michelsen 2002). Much of this disagreement stems from difficulties in accurately observing thin cirrus and from the diverse dynamical and microphysical contexts in which they form. Despite the controversy, the iris effect highlights the sensitivity of Earth's radiative balance to variations in tropical cloud cover, especially those tied to convection, ice microphysics, and precipitation efficiency.

1.3 Land/Ocean Convection

Convection over land and ocean differs across multiple dynamical, thermodynamical, and microphysical dimensions, influencing storm structure, intensity, and precipitation efficiency (PE). In general, deep convection over oceans develops more slowly and exhibits weaker updrafts compared to land-based convection. This difference is largely due to the lower peak vertical velocities observed over oceanic regions (Heymsfield et al. 2010), which arise from the weaker diurnal heating of the sea surface and the absence of strong solar-driven surface forcing. In contrast, land surfaces, with their lower heat capacity and larger diurnal temperature range, can heat rapidly during the day, generating sharper instability and stronger thermals that favor vigorous updrafts and deeper convection. As a result, land-based convection tends to be more intense and vertically developed, particularly during the afternoon when surface heating peaks (Tian et al. 2005). From a microphysical perspective, continental convection is often characterized by more intense updrafts, which promote the production of graupel and hail. While these larger, denser ice particles indicate more extensive glaciation and riming processes, we believe they can also reduce PE, as more condensate is retained aloft and a greater fraction of hydrometeors sublimates or evaporates before reaching the surface.

In contrast, maritime convection, especially within well-organized Mesoscale Convective Systems (MCSs), generally favors stratiform precipitation and efficient warm-rain processes, relying less on ice-based mechanisms. As a result, oceanic MCSs often exhibit higher PE, particularly in environments with deep warm clouds and abundant moisture supplied by the ocean surface (Angulo-Umana and Kim 2023). The vertical structure and longevity of oceanic convection also differ substantially from land-based systems (Matsui et al. 2016). While continental convection is typically impulsive and tightly coupled to the diurnal cycle,

oceanic convection tends to be more persistent, developing over longer timescales and sometimes organizing into large, long-lived MCSs. These systems often feature broader anvils that influence tropical radiative processes, particularly through longwave cloud-radiative effects.

Precipitation efficiency in both land and oceanic convection is strongly modulated by ice-phase processes. In intense continental convection, strong updrafts favor the formation of large graupel and hail, which may remain aloft for extended periods or be lofted above the melting layer, reducing PE as condensate is recycled, sublimated, or evaporated before reaching the surface. In contrast, maritime convection typically produces weaker updrafts and smaller ice particles, which aggregate or melt more efficiently, supporting warm-rain processes and higher PE.

Large-scale climate oscillations, such as El Niño–Southern Oscillation (ENSO), primarily influence oceanic convection in the tropics due to the continuous oceanic moisture supply (Mpheshea et al. 2025). Sea surface temperature anomalies can rapidly modulate convective potential over the oceans, whereas land convection is more strongly influenced by seasonal cycles, topography, and limited moisture availability (Wane et al. 2024). For the period analyzed in this study (2014–2016), ENSO was predominantly in an El Niño phase, which may have enhanced tropical ocean convection relative to continental regions.

1.4 Latitudinal Variations in Deep Convection

The microphysical processes aloft and resulting surface precipitation vary significantly with latitude. In the tropics, convection can be broadly categorized into deep, precipitating clouds and shallow, non-precipitating clouds (Sun and Lindzen 1993; Houze et al. 2015). Tropical convective systems play a central role in Earth's radiative balance, yet their feedbacks remain uncertain. Debate persists over whether these systems provide net positive or negative radiative forcing, a discussion often linked to the hypothesized iris effect, which suggests that reductions in high-level cirrus clouds with warming allow more infrared radiation to escape, acting as a negative feedback on climate (Lindzen et al. 2001; Lin et al. 2002). Observations indicate, however, that the net radiative impact in the tropics may be close to zero due to compensating effects between optically thick, rainy convective cores and optically thinner ice clouds in stratiform anvils (Hartmann et al. 2001). This implies that the observed radiative neutrality arises not from a single cloud type, but from the combined behavior of multiple cloud types produced by tropical deep convection.

Beyond updraft dynamics, entrainment and detrainment play crucial roles in shaping ice microphysical properties. Models indicate that entrainment rates in convective cores are inversely proportional to updraft velocity, influencing ice crystal habits regardless of convective depth (Anber et al. 2019). Korolev et al. (2024) expand on this, demonstrating that high ice water content (HIWC) regions frequently contain ice particles with non-standard habits, influenced by entrainment of aged ice particles from ambient cloud regions (see Figs. 4 and 5). Vertical distributions of ice water content in convective clouds also depend on the partitioning of condensate into precipitation and detrained components. Ice detrainment from deep convection is a major source of upper-tropospheric stratiform anvils, linking convective microphysics to tropical radiative effects (Yuan and Houze 2010; Sokol and Hartmann 2020). The magnitude of this detrained condensate reflects the competition between lofted condensate and material that falls out as precipitation, with snow detrainment supporting stratiform cloud microphysics and enhancing stratiform precipitation associated with the parent convective system (Lin 2021).

Latitudinal differences also influence sensitivity to microphysical processes. Zeng et al. (2009) used long-term cloud-resolving simulations to examine the influence of ice microphysics on top-of-atmosphere (TOA) radiative fluxes across both tropical and midlatitude regions. Their results showed that upper-tropospheric cloud ice content and TOA radiative forcing are more sensitive to variations in ice nuclei concentrations in midlatitudes than in the tropics. This heightened sensitivity has direct implications for PE, as ice nuclei regulate the partitioning of condensate between suspended cloud ice and precipitating hydrometeors. In stratiform and anvil clouds, which are common in midlatitude convection, ice nuclei strongly influence the formation and persistence of small ice crystals, favoring condensate retention aloft and reduced PE. In contrast, convective cores, which are more prevalent in the tropics, are dominated by graupel growth and riming processes that are less sensitive to ice nuclei and more directly linked to efficient precipitation formation. However, evaluating these microphysical pathways remains observationally challenging, as robust separation of stratiform and anvil cloud components is difficult. Accurate identification of anvil clouds is therefore a critical observational constraint for quantifying PE and its radiative impacts across latitudes.

We hypothesize that precipitation efficiency in deep convective systems varies systematically across different convective environments as a result of interactions among storm dynamics, microphysical structure, and environmental conditions. In particular, we expect that differences in hydrometeor vertical distribution,

storm organization, and environmental forcing will be reflected in measurable variations in precipitation efficiency and its components. For example, we anticipate precipitation efficiency to be higher for oceanic convection than land. By comparing convective systems across tropical and midlatitude regions, this study tests whether commonly invoked controls such as latitude, storm type, and large-scale circulation adequately explain PE variability, or whether additional factors related to storm vertical structure, lifecycle, and dynamical support are required to interpret observed differences.

2 Methodology

Quantifying the components of deep convection has been historically difficult, whether through in situ, remote sensing, or modeling perspectives. From an in situ perspective, aircraft are unable to fly and sample the most intense convection due to safety reasons. Remote sensing retrievals often rely on radiation that are either unable to penetrate the deepest convective clouds, or attenuated as a result of condensate (Hemsfield et al. 2010). The use of longer wavelengths can help minimize the latter. Some models have attempted with parameterizing the microphysics of convective updrafts (Elsaesser et al. 2017), but this too proves to be difficult when there is a lack of mathematical explanation to help parameterize convective updraft velocities, which is required for performing physical partitioning of updraft ice water content (IWC). Ice microphysics on its own has proven to be difficult to conclude what conditions and processes a given ice crystal has gone through, due to its microscopic nature. With all of this into account, this research aims to provide meaninful results through the following methodology.

2.1 Instrumentation and Datasets

The use of satellite-based radar observations has significantly advanced our understanding of the vertical structure and spatial organization of deep convective systems, particularly those embedded within MCSs. MCSs are typically composed of two primary components: a convective core, marked by intense, localized updrafts and heavy precipitation, and a broad stratiform region, often extending hundreds of kilometers downwind. Active radar sensors such as those aboard CloudSat and the Global Precipitation Measurement mission (GPM) are especially useful in resolving these structural components. Within convective regions,

high radar reflectivity values often indicate the presence of graupel and hail, product of vigorous updrafts lofting large hydrometeors into the upper troposphere. In contrast, weaker reflectivity signatures in stratiform regions represent widespread light precipitation and ice-phase particles, including snow and horizontally advected ice crystals, which are detrained into the anvil cloud and may sublimate or evaporate before reaching the surface. Importantly, radar observations allow researchers to disentangle microphysical and dynamical processes within MCSs by observing vertical profiles of reflectivity, hydrometeor classification, and storm depth. Past satellite-based studies have made significant strides in identifying and characterizing the nonprecipitating anvil clouds associated with tropical convection, which are difficult to observe using ground-based instruments or passive sensors alone (Yuan and Houze 2010; Hartmann et al. 2010). These anvil clouds, while not contributing directly to surface rainfall, play a key role in modulating the Earth's radiation budget by reflecting solar radiation and trapping outgoing longwave radiation.

Despite the advantages of spaceborne radar systems, including their ability to observe remote and oceanic regions with uniform global coverage, there are temporal limitations. Because sensors like CloudSat operate in sun-synchronous orbit, any given location is typically observed only a few times per day, which poses challenges for capturing the full life cycle of convective systems. GPM poses a different, yet similar issue, which has a precessing orbit and a narrow swath that only samples a few times per day, and rarely observes the same storm more than once This temporal sparsity limits the ability to resolve rapid storm evolution or diurnal variability. However, this is partially resolved by the shear number of stroms sampled over the duration of these missions (Liu et al. 2020). Statistical analyses of many storms can provide important insights into global PE variations.

2.1.1 CloudSat

CloudSat, launched in 2006 as a part of NASA's A-Train satellite constellation, enhanced precipitation measurement by providing the first spaceborne 94 GHz Cloud Profiling Radar (CPR), capable of penetrating deep into cloud systems (Stephens et al. 2022). The A-Train constellation is made up of five other weather tracking satellites to CloudSat. Passive sensors only infer cloud properties from top-of-atmosphere radiances, whereas CloudSat's active radar retrieves detailed vertical profiles of cloud reflectivity, offering direct insights into the structure and intensity of precipitating clouds. This makes CloudSat most effective at detecting

light precipitation and small ice particles, distinguishing between cloud types and being able to characterize the vertical extent of hydrometeors including snow, graupel, and ice crystals aloft. It has a sensitivity reaching approximately -30 dBZ which allows it to observe ice clouds and stratiform precipitation, which can be missed by larger wavelength radars. CloudSat is especially useful for studying tropical convection as it captures both convective cores and their associated anvil outflows, helping to evaluate the distribution and microphysical evolution of precipitation processes in the upper and middle troposphere. It should be noted that although the CPR has a difficult time detecting near-surface rainfall due to the ground clutter in the lowest 1km (Liu et al. 2015), it provides unparalleled information within the upper portions of our atmosphere, which is crucial for predicting future climate dynamics. Furthermore, this limitation can be overcome by using other satellite missions, such as GPM, complementary to get a better picture of convective systems, which will be discussed more later on. Beyond its utility in precipitation profiling, CloudSat has been instrumental in advancing our understanding of the radiative effects of clouds (L'Ecuyer et al. 2008), specifically high clouds associated with deep convection. By providing vertical profiles of cloud structure and hydrometeor phase, CloudSat enables more accurate estimate of cloud radiative heating rates throughout the given atmospheric column (L'Ecuyer et al. 2008). This is particularly important for quantifying the shortwave (SW) and longwave (LW) components of the net CRE. High, optically thick clouds, such as those formed in deep convective systems, strongly reflect incoming solar radiation and subsequently cooling the Earth's surface while simultaneously trapping outgoing infrared radiation which in turn warms in the atmosphere. CloudSat observations enable a three-dimensional characterization of clouds that is essential for diagnosing their net impact on Earth's energy budget. In particular, understanding how anvil clouds and stratiform outflow layers modify LW fluxes at the top of the atmosphere can help reduce uncertainties in tropical cloud feedbacks under climate change.

2.1.2 GPM

The Global Precipitation Measurement (GPM) mission launched in 2014 as a successor to the Tropical Rainfall Measuring Mission (TRMM) and provides a global view of precipitation. GPM carries two key instruments: the Dual-Frequency Precipitation Radar (DPR) and the GPM Microwave Imager (GMI). The DPR includes both Ku-band (13.6 GHz) and Ka-band (35.5 GHz) radars, enabling it to resolve precipitation

intensity, structure, and type with greater accuracy than TRMM. The dual-frequency capability allows the DPR to probe precipitation microphysics more deeply by exploiting differences in scattering and attenuation between the two frequencies (Gao et al. 2017). This enables more accurate retrievals of hydrometeor size distributions, vertical structure of precipitation, and discrimination between liquid, mixed-phase, and frozen precipitation. Compared to TRMM's single-frequency radar, DPR provides higher sensitivity to light rain and snow, as well as improved detection of shallow precipitation systems common at higher latitudes. The GMI is a conically scanning microwave radiometer with 13 channels spanning frequencies from 10 GHz to 183 GHz. Its broad frequency coverage makes it sensitive to wide spectrum of atmospheric processes: low-frequency channels capture emission signatures from liquid precipitation and ocean surface winds, while high-frequency channels detect scattering from frozen hydrometeors such as graupel and snow.

GPM's expanded latitudinal coverage and improved sensitivity to light precipitation and falling snow make it particularly valuable for studying a wide range of precipitation regimes, including those at higher latitudes and over oceans. However, while CloudSat provides detailed vertical profiles of hydrometeors and cloud layers with high vertical resolution, it suffers from limited temporal coverage due to its narrow nadir track and sparse sampling (Stephens et al. 2002). GPM, however, offers near-global, high frequency observations of precipitation with a broader swath, making it ideal for capturing the spatial variability of convective systems. When used in tandem, CloudSat and GPM offer a more complete picture of precipitating cloud systems by enhancing out ability to diagnose the coupling between cloud microphysics, updraft dynamics, and the radiative effect of deep convective systems, which is crucial for understanding their role in the climate system (Turk et al. 2021; Hayden and Liu 2018).

2.1.3 CloudSat/GPM Coincidence Dataset

To facilitate detailed comparisons between active satellite measurements of cloud and precipitation properties, a coincidence dataset between CloudSat and GPM was curated by Turk et al. (2021), which matches observations from the CPR on CloudSat with those from the DPR and GMI from the GPM mission. This dataset identifies times and locations where CloudSat and GPM overpasses occur within close spatial and temporal proximity, typically within minutes and tens of kilometers, allowing a near-simultaneous cross-validation of vertical cloud structure, precipitation profiles, and hydrometeor phase. The dataset includes

matched geolocation, timing, radar reflectivity, and radiometer data from both missions, enabling studies that leverage CloudSat's sensitivity to cloud ice and GPM's strength in detecting precipitation processes. It is especially valuable for evaluating differences in radar sensitivity, assessing retrieval consistency across platforms, and improving microphysical parameterizations in models. The Turk et al. (2021) dataset provides a powerful look for researchers studying precipitation efficiency, cloud vertical structure, and cloud-radiation interactions on both regional and global scales, yet has been underused, especially regarding PE.

The core of Turk et al.'s approach is to identify coincident overpasses where CloudSat and GPM observe nearly the same atmospheric column within a cloud temporal and spatial window. Typically, a temporal threshold of +/- 15 minutes and a spatial threshold of less than 20-30 km are applied to ensure minimal atmospheric evolution between observations. CloudSat's narrow nadir-pointing track is matched against the broader GPM swath using high-resolution orbital geometry and altitude data, allowing the interpolation of GPM radar and radiometer data to the CloudSat ground track. Once matched, the dataset preserves key geophysical parameters from each platform, while also including auxiliary variables, such as cloud classification flags, convective/stratiform identifiers, and quality control masks. To ensure consistency, Turk et al.'s methodology applies strict orbit synchronization, geolocation correction, and environmental screening (i.e., over ocean vs. land, or filtering by latitude bands). The resulting dataset enables direct, pixel-level comparisons between CloudSat and GPM observations, making it a powerful tool for evaluating the performance of retrieval algorithms, validating precipitation and cloud ice products, and studying vertical hydrometeor structure across a range of cloud regimes. CloudSat CPR provides high-vertical-resolution profiles (240–500 m) with a fine horizontal footprint of 1.4 km $\times$ 1.7 km, while the GPM DPR measures precipitation with a coarser horizontal footprint of 5 km and vertical resolution of 125–250 m. By matching these measurements in space and time, the coincidence dataset allows for near–true pixel-level comparisons, improving our ability to diagnose the coupling between cloud microphysics, updraft dynamics, and the radiative effect of deep convective systems. These characteristics make the dataset uniquely suited for research into cloud microphysics, precipitation efficiency, and cloud–radiation interactions.

2.1.4 Convective Object Database

This work uses satellite-based retrievals from a CloudSat and GPM coincidence dataset colocated with a Convective Object (CO) database developed by Pilewski and L'Ecuyer (2025). The CO database identifies and characterizes convective systems globally from August 2006 through December 2016 using observations from multiple A-Train sensors, enabling detailed evaluations of cloud microphysics, vertical structure, and associated large-scale environments. Convective Objects are classified using a combination of cloud-top height, local reflectivity peaks, and the relative center of gravity (rCoG), which measures the altitude of the condensate-weighted center of mass relative to the melting layer. Systems with rCoG values ≥ 4 km above the melting level are considered to exhibit strong vertical development and vigorous updrafts, while lower values represent more weakly developed convection (Pilewski and L'Ecuyer 2025).

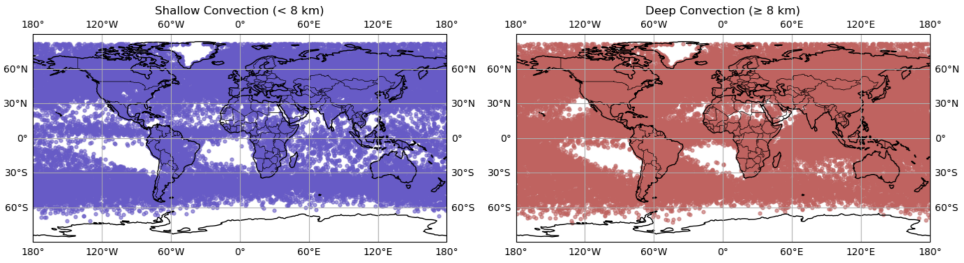

Figure 1: Global distribution of convective events from 2014-2016 from Pilewski and L'Ecuyer 2025 Convective Object Database. Blue dots represent shallow convection, red dots represent deep convection.

CloudSat convectivce objects were identified using the CloudSat 2C-PRECIP-COLUMN convective flag (`Conv_Strat_Flag`), where footprints with more than five convective bins were classified as convective systems. These systems were subsequently matched to COs in the database based on temporal coincidence and spatial proximity within 1° latitude or longitude. Figure 2 shows the resulting distribution of matched cases, separated into shallow and deep categories following the CO classification scheme. In accordance with the CO database definition, deep convection is defined as systems with cloud-top heights ≥ 8 km and rCoG ≥ 4 km above the melting layer. Only systems meeting these criteria are examined in this study to ensure consistency with the CO framework. Shallow convective systems, defined as those with cloud-top heights < 8 km or insufficient vertical development (rCoG < 4 km), are not included in the analysis here due to

time limitations, but may be considered in future work.

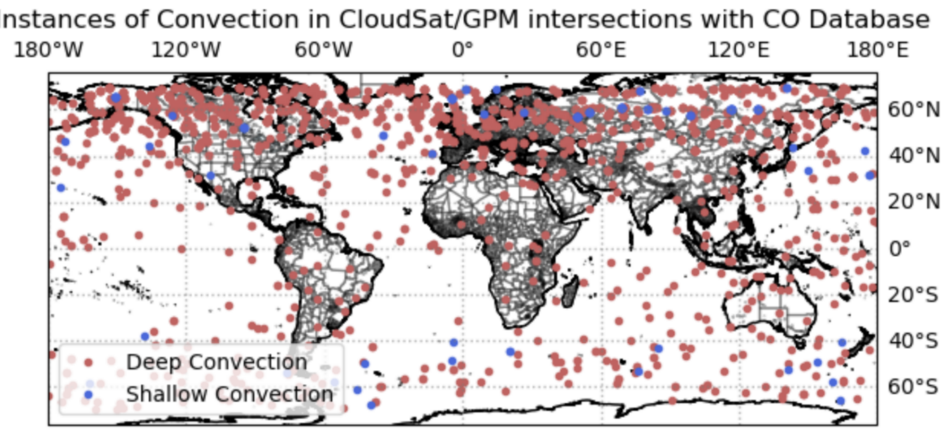

Figure 2: Instances of convection from CloudSat/GPM coincidence (Turk et al. 2021) dataset that also have corresponding points within Pilewski and L'Ecuyer 2025 Convective Object Database for the years 2014-2016. Red dots represent deep convection, blue dots represent shallow convection.

For this research, six case studies were chosen and analyzed in various parts of the world. This was done in order to use observational data to gain more insight on the conditions surrounding deep convection and their resulting precipitation efficiency to gain understanding on the processes that govern both the radiative and hydrological impacts across the globe, and in a changing climate. Four of the six case studies (Cases 3-6) as seen in Fig. 3 were chosen based on the known areas of mass convergence and subsidence due to the Walker Circulation (Hosking et al. 2012), with two (Cases 5 and 6) representing the main ascending and descending branches of the circulation. The Walker Circulation is a large-scale atmospheric circulation pattern that occurs along the equator, primarily in the tropical Pacific Ocean. It plays a key role in global weather and climate influencing trade winds, precipitation and ocean temperatures (Chand et al. 2023). Generally, warm waters in the western Pacific cause air to rise due to convection, the air eventually cooling and moves eastward in the upper troposphere, eventually sinking over the eastern Pacific, where the SSTs are cooler. It should also be noted that global oscillations such as El Nino and La Nina influence the Walker Circulation by either, respectively, reversing or weakening it, or intensifying it (Chand et al. 2023). The remaining two case studies in Fig. 3 were chosen at the mid-latitudes both in the Northern and Southern Hemispheres, hoping to latitudinal differences. The goal of these case studies as a whole is to evaluate the

differences not only latitudinally, but to also gain insight on land/sea variations. This work also evaluates global trends in precipitation efficiency in order to get an overall sense of what are the most important factors in deciding the amount of water that reaches the ground. Finally, due to the already discussed latitudinal patterns of convection, it should be considered that the midlatitude cases will have less statistical data within their regional boxes, due to the inherent abundance of convection in the tropics. However, this should not be a limitation of the study, due to there still being hundreds of data points within these regions.

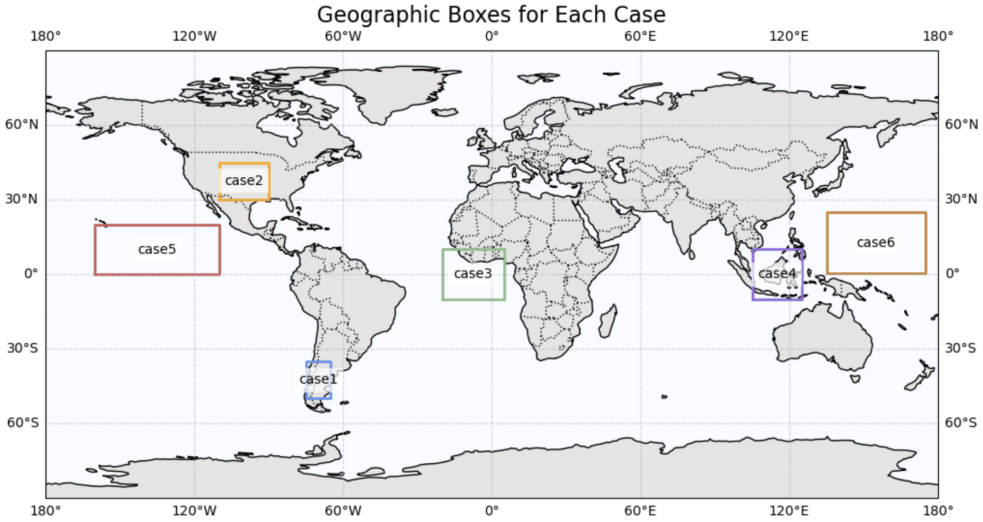

Figure 3: Regional boxes from which each case study represents, and where global statistics are calculated within

2.2 Calculations

2.2.1 Ice Water Path

CloudSat's 2C-ICE product provides the primary retrieval of ice water content (IWC) and its vertical integral, the ice water path (IWP), using a combined radar–lidar optimal estimation framework developed by Deng et al. (2015). CALIPSO, a lidar satellite in NASA's A-Train constellation, carries the Cloud-Aerosol Lidar with Orthogonal Polarization (CALIOP) which provides high-vertical-resolution measurements of cloud and aerosol backscatter, offering detailed observations of cloud top heights, thin cirrus layers, and the vertical distribution of ice and liquid particles that are often undetectable by radar alone. The retrieval algorithm for

IWP combines CloudSat CPR reflectivity and CALIPSO lidar backscatter to infer profiles of IWC throughout the column. Because neither sensor alone can fully observe all ice particle sizes or cloud depths, the algorithm uses optimal estimation to incorporate observational uncertainties, a priori microphysical constraints, and a forward model that simulates radar and lidar signals from candidate IWC profiles. The resulting state vector provides the most probable IWC profile given both the measurements and physical constraints.

Once IWC is retrieved at each vertical level, IWP is computed as the vertical integral of IWC over the cloud depth:

$$\mathrm{IWP} = \int_{z_{\mathrm{base}}}^{z_{\mathrm{top}}} \mathrm{IWC}(z)\, dz \tag{1}$$

where $\mathrm{IWC}(z)$ is the ice water content at height z with units of $\mathrm{g\,m^{-3}}$, and z_{base} and z_{top} represent the cloud-base and cloud-top heights, respectively. In the 2C-ICE product, IWC is reported at CloudSat's native 240-m vertical resolution, and the standard output variable for IWP is included as the vertically integrated value in units of $\mathrm{kg\,m^{-2}}$. This radar–lidar synergy enables improved sensitivity to both large precipitating ice particles (from radar) and smaller, high-altitude ice crystals (from lidar), making 2C-ICE one of the most robust global satellite datasets available for quantifying IWC and IWP (Deng et al. 2013; Deng et al. 2015).

2.2.2 Liquid Water Path

In this study, liquid water path (LWP) is retrieved from the Advanced Microwave Scanning Radiometer 2 (AMSR2), which is also a part of the A-Train Constellation. AMSR2 provides a well-established passive microwave retrieval of cloud liquid water over ocean surfaces, leveraging its suite of low-frequency microwave channels (6–37 GHz), which are highly sensitive to cloud liquid water through absorption and emission processes. Because liquid cloud droplets act primarily as emitters at these wavelengths, increases in column liquid water produce measurable increases in brightness temperature, enabling robust retrievals of LWP in non-precipitating and lightly precipitating conditions (Stephens et al. 2018).

AMSR2 LWP is derived using an optimal estimation framework that minimizes the mismatch between observed and simulated brightness temperatures (Chang et al., NOAA Technical Document). The retrieved

atmospheric state vector $\hat{\mathbf{x}}$ is obtained by solving

$$\hat{\mathbf{x}} = \arg\min_{\mathbf{x}} \left\{ \left[\mathbf{T}_b^{\text{obs}} - \mathbf{F}(\mathbf{x})\right]^{\mathrm{T}} \mathbf{S}_\epsilon^{-1} \left[\mathbf{T}_b^{\text{obs}} - \mathbf{F}(\mathbf{x})\right] + \left[\mathbf{x} - \mathbf{x}_a\right]^{\mathrm{T}} \mathbf{S}_a^{-1} \left[\mathbf{x} - \mathbf{x}_a\right] \right\}, \tag{2}$$

where $\mathbf{F}(\mathbf{x})$ is the forward radiative transfer model, $\mathbf{x}_a$ is the a priori atmospheric state, and $\mathbf{S}_\epsilon$ and $\mathbf{S}_a$ are the measurement and a priori error covariance matrices. In this retrieval, LWP is taken directly from the liquid component of the state vector. Over ocean surfaces where surface emissivity is well understood and highly constrained, AMSR2 provides stable and widely validated LWP estimates suitable for climatological and process-level analysis (Elsaesser et al. 2017, Greenwald et al. 2018)

AMSR2's consistent sampling, sensitivity to cloud liquid water, and long-term calibration stability make it well suited for analyzing liquid water variability within this case study. No radar-based constraints are used in the retrieval, and the passive microwave–only approach ensures that the LWP values reported here correspond to the full column liquid water inferred directly from AMSR2 brightness temperature observations (Lebsock et al. 2014; Zhao et al. 2015).

2.2.3 Rain Rate

Rain rate used for the precipitation efficiency calculation is obtained primarily from the GPM Dual-Frequency Precipitation Radar (DPR). The DPR provides the most direct satellite-based measurement of rainfall over the tropics and subtropics, retrieving precipitation rate from its Ku- and Ka-band reflectivity profiles and exploiting the complementary sensitivities of the two wavelengths (Hou et al. 2014). A key component of the dual-wavelength retrieval is the dual-frequency ratio (DFR), defined as

$$\text{DFR} = Z_{Ku} - Z_{Ka}, \tag{3}$$

which quantifies the differential attenuation and scattering between the two frequencies. Because the Ka band attenuates more strongly than the Ku band, the DFR provides information on hydrometeor size and path-integrated attenuation, thereby improving constraints on the drop size distribution and vertical structure of precipitation.

In the DPR Level-2 algorithm, rain rate R is estimated by inverting the radar reflectivity–rainfall rela-

tionship

$$Z = aR^b, \tag{4}$$

where Z is the attenuation-corrected reflectivity and a and b are parameters derived from microphysical assumptions and evaluated against ground-based radar. By combining attenuation-corrected reflectivity with dual-frequency constraints such as the DFR and the surface reference method, the DPR retrieval more effectively separates attenuation effects from intrinsic reflectivity, yielding more accurate rain rates in both stratiform and convective regimes.

When DPR coverage is unavailable, either due to swath gaps or low-sensitivity precipitation, rain rate is supplemented with retrievals from AMSR2 using the Goddard Profiling Algorithm (GPROF). GPROF is a Bayesian retrieval framework that estimates precipitation rate by comparing observed brightness temperatures to a large database of simulated atmospheric profiles (Kummerow et al. 2015). The posterior-mean rain rate is computed as

$$\hat{R} = \sum_{i=1}^{N} r_i \, P(r_i \mid \mathbf{T}_b^{\text{obs}}), \tag{5}$$

where r_i is the rain rate associated with the i-th candidate profile in the database, and $P(r_i \mid \mathbf{T}_b^{\text{obs}})$ is the Bayesian posterior probability that the profile produced the observed brightness temperatures $\mathbf{T}_b^{\text{obs}}$. This probability combines the likelihood of observing the brightness temperatures for each candidate profile with the climatological prior distribution of hydrometeor profiles derived from cloud-resolving model simulations and matched radar–radiometer observations. GPROF performs well over ocean surfaces, where microwave emissivity is well characterized, but becomes more uncertain in scenes with strong ice scattering or highly variable surface emissivity (Elsaesser et al. 2015).

In this analysis, DPR rain rates are used whenever available due to their direct physical measurement and high vertical sensitivity. AMSR2/GPROF rain rates provide complementary coverage, ensuring consistent sampling across the study region and preventing gaps in the precipitation efficiency calculation when DPR observations are missing or insufficiently constrained.

For the rain rate used to calculate the precipitation efficiency, GPROF rain rates are used. The primary goal of this algorithm was to correct systematic biases over the Intertropical Convergence Zone (ITCZ), due to the frequent overestimation of precipitation (Kummerow et al. 2001). This algorithm implements

a Bayesian inversion, using prior probability distributions of rain profiles from both cloud-resolving models and radar/radiometer data, along with the likelihood of brightness temperature observations given those profiles (Kummerow et al. 2015). Equation 5 computes the expected rainfall rate:

$$RR = \sum_i r_i \cdot P(r_i \mid \mathrm{BT}_o) \tag{6}$$

Where $P(r_i \mid BT_o)$ comes from the Bayesian inference found in Elsaesser and Kummerow (2015), overall representing the likelihood each profile in the database produced the observed signal. r_i represents the candidate rainfall rate from the training set of known atmospheric profiles with associated simulated brightness temperatures. T_o is the vector of observed brightness temperatures from the satellite sensor at different microwave frequencies.

Numerous validation studies support the interchangeability of rain-rate retrievals from GPM DPR and AMSR2, particularly over oceanic regions and in climatological studies. For instance, You et al. (2020) evaluated Level-2 precipitation estimates from multiple passive microwave radiometers against DPR and found that the spatial patterns and magnitudes of rain-rate estimates align closely across instruments when averaged over large scales They reported agreement within the expected uncertainties for moderate rain-rate regimes, indicating that the passive microwave retrievals and DPR radar estimates capture the same underlying precipitation signal. Moreover, other cross-validation studies have demonstrated that DPR and passive-microwave rain-rate retrievals exhibit similar error statistics in tropical and subtropical oceanic environments (Biswas et al. 2018; Gao et al . 2017). Given these findings, using DPR as the primary rain-rate source and supplementing with AMSR2 when DPR coverage is unavailable provides both spatial completeness and methodological consistency for our PE calculations. The two datasets are thus considered sufficiently compatible for our study's purposes, provided that any known instrument-specific biases are accounted for in the analysis.

2.2.4 Precipitation Efficiency

In this study, precipitation efficiency is defined as the ratio of surface rainfall rate to the total condensate in the atmospheric column, expressed as

$$PE = \frac{RR}{\text{IWP} + \text{LWP}} \tag{7}$$

This formulation treats the LWP and IWP as the column-integrated condensate reservoir from which precipitation is ultimately derived. The inclusion of IWP is particularly important in deep tropical convection, where a substantial fraction of condensate resides in frozen hydrometeors that later melt and contribute to surface rainfall. Incorporating both phases therefore provides a more physically complete representation of the cloud's condensate budget and avoids biases toward warm-rain microphysical regimes.

Numerous definitions of precipitation efficiency exist in both the observational and modeling literature, reflecting differing emphases on microphysical pathways, environmental conditions, and cloud-system energetics. Early theoretical studies often defined PE as the fraction of condensed water that reaches the surface as precipitation (Sui et al. 2007), typically expressed as

$$\frac{\partial [q_v]}{\partial t} = [\text{CONV}\, q_v] + E_s - [S_I q_v] + [S_O q_v] \tag{8}$$

Where the variables represent:

$[q_v]$: Vertically integrated water vapor mixing ratio (kg m^{-2})

$[\text{CONV}\, q_v]$: Convergence of water vapor due to advection (kg m^{-2} s^{-1})

E_s : Surface evaporation rate (kg m^{-2} s^{-1})

$[S_I q_v]$: Integrated source of water vapor (e.g., condensation, deposition) (kg m^{-2} s^{-1})

$[S_O q_v]$: Integrated sink of water vapor (e.g., evaporation of cloud particles) (kg m^{-2} s^{-1})

Cloud-resolving and large-eddy modeling studies adopt related definitions based on the ratio of precipitation production to condensation or deposition (Tao et al. 2004), emphasizing the instantaneous conversion efficiency of vapor to precipitation. Observationally based approaches frequently use column water vapor as

the denominator.

$$PE_{\text{moist}} = \frac{RR}{\text{PW}}, \tag{9}$$

where PW is precipitable water. While useful for large-scale moisture-budget analyses, this definition does not isolate cloud microphysical processes and can obscure the roles of ice and mixed-phase hydrometeors.

The definition adopted here differs from these approaches by explicitly using condensate loadings (LWP + IWP) to represent the state of the cloud rather than its moisture environment or instantaneous condensation rates. This condensate-based PE provides a direct observational analog to microphysical efficiencies computed in modeling frameworks while remaining grounded in satellite-retrieved quantities. Because IWP can dominate the condensate budget in convective systems, especially in regions influenced by strong updrafts and large-scale ascent, including ice contributions enables a more accurate assessment of the column's ability to convert stored condensate into precipitation. This makes the metric particularly well suited for diagnosing case-to-case variability in convective intensity, microphysical regimes, and large-scale environmental forcing in tropical cloud systems.

As with any satellite-derived quantity, precipitation efficiency inherits uncertainties from both the numerator (RR) and denominator (LWP + IWP). Passive microwave rainfall retrievals exhibit typical random errors of 10–25% in non-precipitating and light-rain conditions, increasing to 30–50% in deep convection due to ice scattering and surface emissivity ambiguities (Kummerow et al. 2015). LWP retrievals from GMI and AMSR2 carry uncertainties on the order of 15–30% over ocean (Elsaesser et al. 2017), while CloudSat 2C-ICE IWP retrievals commonly exhibit uncertainties of 25–50% depending on particle habit assumptions and radar–lidar synergy constraints (Deng et al. 2013). Because these errors propagate nonlinearly through the PE ratio, individual PE values may contain substantial case-specific uncertainty, which can be difficult to quantify.

2.2.5 Cloud Radiative Effect

Cloud radiative effect (CRE) is used in this study to quantify how clouds modify the Earth's radiative energy budget relative to clear-sky conditions, following the definition established in Henderson and L'Ecuyer (2013). CRE is computed using radiative flux profiles from the CloudSat 2B-FLXHR-LIDAR product, which

simulates broadband shortwave and longwave fluxes under both all-sky (cloud-present) and clear-sky states. As shown in Equation 9, CRE is defined as the difference between all-sky and clear-sky radiative fluxes at either the top of the atmosphere or the surface, encapsulating the net impact of clouds on the reflection, absorption, and emission of radiation:

$$\mathrm{CRE} = F_{\text{all-sky}} - F_{\text{clear-sky}}. \tag{10}$$

Shortwave CRE primarily reflects cloud albedo and solar reflection, whereas longwave CRE captures cloud-top emissivity and the trapping of terrestrial radiation. Although conceptually straightforward, the magnitude of CRE depends strongly on cloud vertical structure, microphysical properties, and the surrounding thermodynamic environment, making it sensitive to retrieval assumptions (Yan et al. 2021). The 2B-FLXHR-LIDAR product inherits uncertainties from upstream CloudSat and CALIPSO cloud property retrievals, including particle size assumptions, optical depth estimates, and lidar attenuation corrections, all of which propagate through the radiative transfer calculations. These uncertainties can introduce biases in both shortwave and longwave CRE, particularly for deep convection, multilayer cloud systems, and scenes containing substantial ice content. Nevertheless, despite these limitations, the CRE formulation remains a widely applied metric for quantifying cloud-radiation interactions and provides a consistent framework for evaluating radiative impacts across regimes and relating them to variations in precipitation efficiency and cloud microphysical states.

3 Results and Discussion of Case Studies

3.1 Subtropical Deep Convection

3.1.1 October 16th, 2016: Argentina, east of the Andes Mountains

The first case analyzed occurred over central Argentina on October 16th, 2016. Convection in this region is among the most vigorous globally, particularly within the La Plata Basin and the Sierras de Córdoba, which together form one of the strongest non-tropical convective hotspots. This environment is shaped by

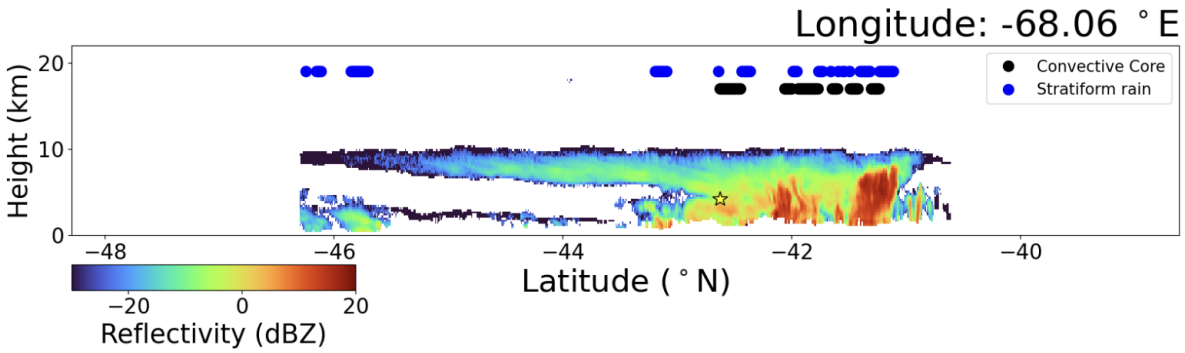

Figure 4: CloudSat reflectivity profile for Case 1:October 16th 2016, over Argentina. Black dots indicate the location of a convective core, while blue represent stratiform rain. Star is representative of the rCoG altitude for any given convective core associated with the system

a combination of deep low-level moisture supplied by the Amazon Basin and the Atlantic Ocean, funneled southward by the South American Low-Level Jet (SALLJ); strong orographic lifting along the Sierras; and upper-level troughs propagating eastward from the Pacific that enhance dynamic ascent (Romatschke and Houze 2010). As a result, MCSs frequently initiate over the terrain and propagate eastward as long-lived, highly organized convective complexes. Observational and radar studies show that subtropical South America, particularly near the Sierras de Córdoba and adjacent plains, frequently hosts extremely deep convective storms, with intense updrafts, frequent large hail and expansive anvil and stratiform cloud shields (Rasmussen et al., 2014; Kumjian et al., 2020). Although peak convective activity occurs in austral summer, strong MCSs are common in October as moisture and instability begin to increase.

The CloudSat overpass captures a system consistent with these environmental conditions. The reflectivity structure (Fig. 4) reveals multiple convective cores embedded within a broader anvil extending to roughly 10 km, with elevated reflectivity values aloft indicative of abundant or sizable ice particles. These signatures contrast with the comparatively modest rain rates along the track (Fig. 6), suggesting strong lofting of hydrometeors and a significant retention of ice in the upper cloud. The system is also characterized by substantial upper-level vertical wind shear (Fig. 5), which strongly influences storm organization and anvil shape. High shear in this region is climatologically expected due to the interaction between blocked low-level flow east of the Andes and persistent upper-level westerlies from the subtropical jet. This shear facilitates

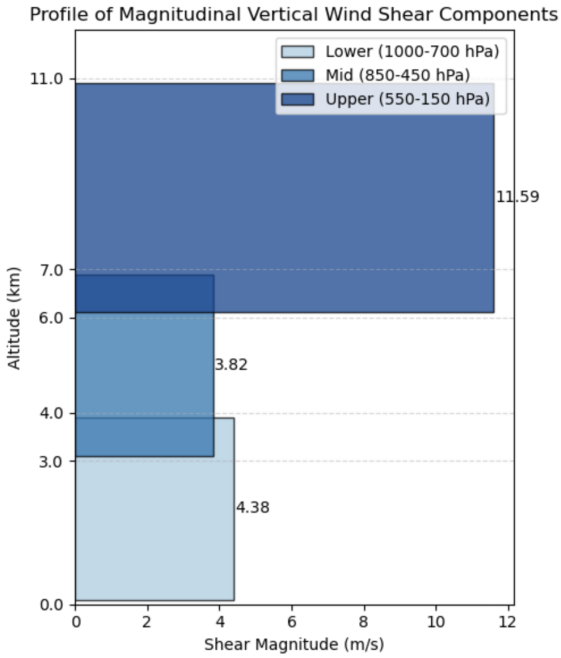

Figure 5: ECMWF lower (1000-700 hPa), middle (850-450 hPa) and upper (550-150 hPa) level shear magnitudes for Case 1: October 16th, 2016, over Argentina.

the horizontal advection of ice away from updraft cores, broadening the anvil and enhancing its radiative footprint. While this can reduce local precipitation efficiency by transporting ice away from its growth region or into drier environmental layers, it simultaneously promotes expansive, radiatively significant cloud shields.

Although liquid water content appears uniformly distributed in magnitude across the system 9 (Fig. 7), convective core or not, ice water content is most heavily concentrated in the areas of most intense convection, and is relatively low, but still apparent, in the anvil region. Furthermore, when the zonal mean is taken of the ice and liquid water contents, it is apparent that the liquid in this system is most prevalent at lower altitudes with the highest water contents, whereas liquid ice is most dominated by smaller ice water contents higher in the atmosphere. Interestingly, there is a gradual increase in the ice water content as altitude increases, multiple kilometers where values stay approximately stagnant, and then a gradual decrease at approximately 7 kilometers. These values of constant IWC can be explained due to limiting saturation available for available water molecules, detrainment of cloud material feeding into the anvil, or a balance between ice growth and

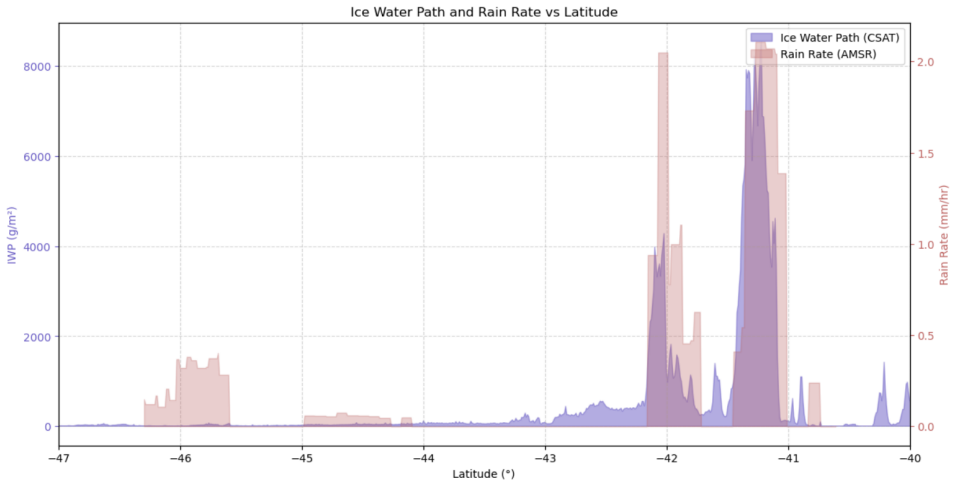

Figure 6: Ice water path (blue) in $\mathrm{g\,m^{-2}}$ and rain rate (red) in $\mathrm{mm\,hr^{-1}}$ for Case 1 in Argentina. Ice water path is provided by CSAT and rain rate is provided by AMSR.

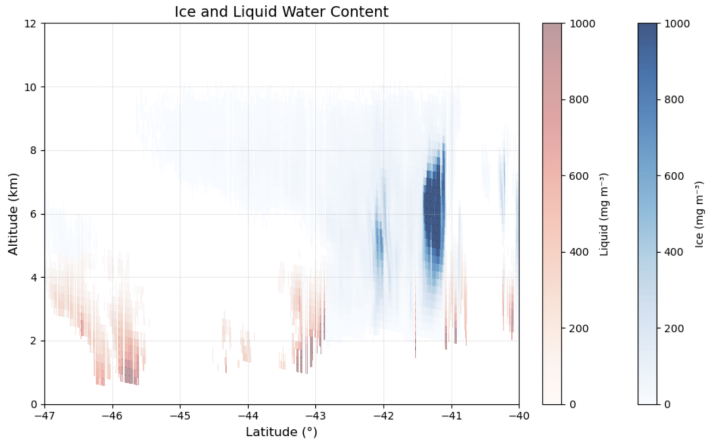

Figure 7: Ice (blue) and liquid water (red) contents over the CloudSat curtain associated with the Case 1 convective object located in Argentina.

fallout if the the system's updraft is not strong enough to keep all particles aloft as new particles begin to form. The subsequent decrease in occurring in the stratosphere could be due to the boundary changes between the troposphere and stratosphere, where vertical motion commonly weakens. Another possible explanation could be that the stratosphere is stable and dry, which is not favorable for keeping ice aloft. The radiative influence of this system (Fig. 8) can be characterized as net cooling, especially in regions of high

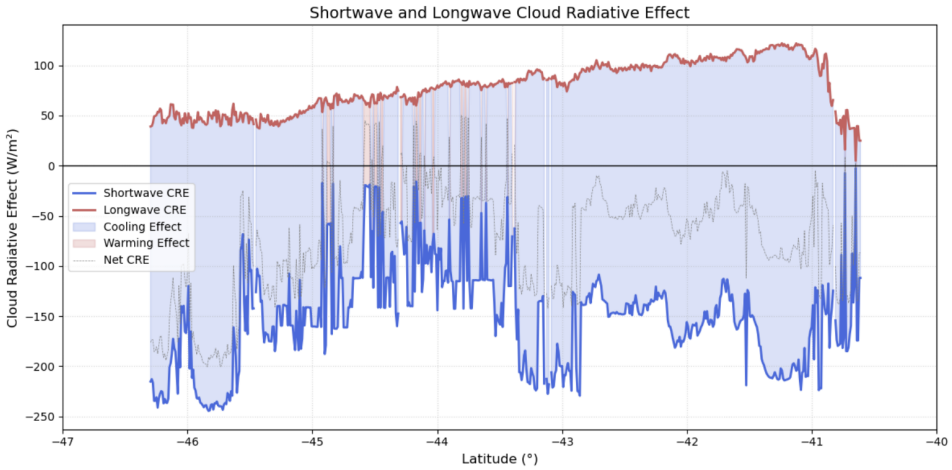

Figure 8: Net cloud radiative effect (CRE) represented by gray line, red line associated with longwave CRE, blue associated with shortwave CRE. Shading corresponds to a net warming (red) effect, or a net cooling (blue) effect in the Case 1 convective object.

rainfall and high ice water path. This system is mostly dominated by shortwave CRE, meaning the regions of highest reflectivity, as well as most of the anvil region are optically thick enough to reflect incoming sunlight back into space. The instances of warming in the anvil can be explained through the Stefan-Boltzmann law, detailing that high, cold anvil clouds emit less LW radiation upward due to their low temperatures. Furthermore, from below, they also trap outgoing LW radiation from the surface and lower troposphere.

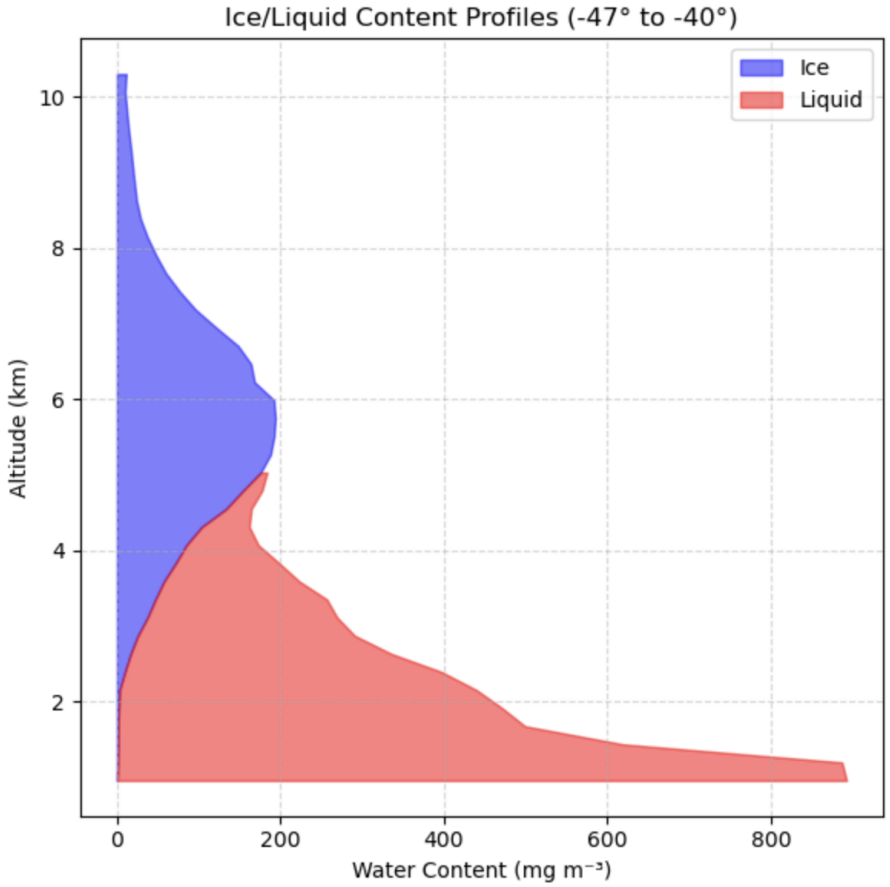

Figure 9: Zonal mean of ice (blue) and liquid (red) water content profiles, water content values in $\mathrm{mg\,m^{-3}}$

The analysis of the Argentina case reveals a vertically deep, highly sheared convective system consistent with the extreme MCS environments characteristic of the La Plata Basin. The reflectivity structure shows multiple convective cores surrounded by a broad anvil extending to approximately 10 km, with values exceeding 20 dBZ at mid-levels, suggesting the presence of large or abundant ice particles. Despite this, rain rates along the CloudSat track remain relatively low, indicating inefficient conversion of condensate to precipitation, which is consistent with early lifecycle convection where significant ice lofting reduces available LWP for rain formation. Strong upper-level wind shear is evident in Figure 5, promoting horizontal advection of hydrometeors and contributing to the widespread anvil. This shear-induced detrainment likely enhances IWP

while limiting local precipitation efficiency by displacing ice far from the updraft core. Vertical hydrometeor profiles further support this interpretation: liquid water content peaks at low levels in convective cores, while ice water content dominates at higher altitudes, increasing gradually with height before decreasing near the tropopause, consistent with decreasing saturation and weakened vertical motion. Radiatively, the system generates a net cooling effect dominated by shortwave CRE, as the optically thick anvils reflect substantial incoming solar radiation. Localized LW warming occurs beneath the anvil due to trapping of upwelling terrestrial radiation, but the shortwave component dominates the overall energy balance. Taken together, these structural, microphysical, and radiative characteristics support the interpretation that this CloudSat overpass captured the system earlier in its lifecycle, when intense updrafts and strong shear favor ice export and anvil production but before the convective system has matured into a highly efficient rain-producing state.

3.1.2 September 29th, 2014: United States Great Plains

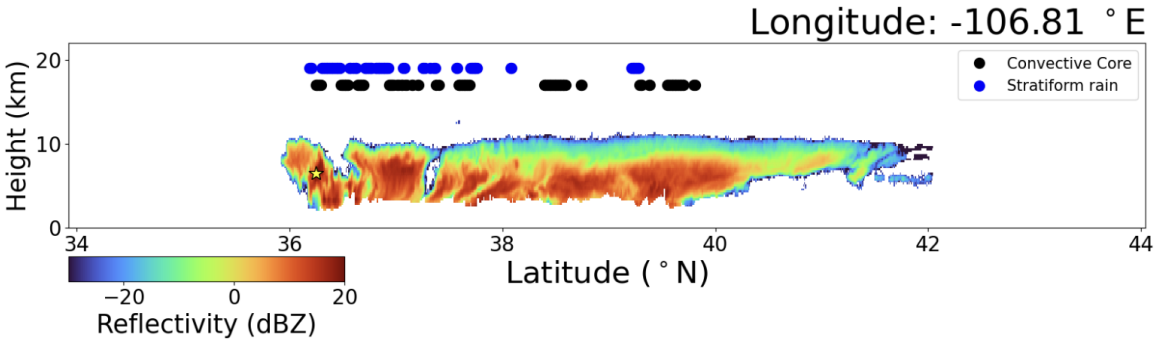

Figure 10: As in figure 4, regarding the September 29th, 2014 case over the Great Plains

The Great Plains is one of the most studied and active regions for continental deep convection on Earth. The forcing mechanisms in this region are often triggered by strong synoptic and mesoscale forcing rather than thermodynamic ascent like in the tropics. The Great Plains low-level jet (LLJ) transports warm, moist air from the Gulf of Mexico northward at night (Higgins et al., 1997), forming dryline boundaries where the moist Gulf air meets hot, dry continental air from the desert southwest, allowing convective initiation.

Frontal systems and upper-level troughs provide strong lift and vertical wind shear to organize convective systems further. Convection in the Great Plains is often explosive and intermittent, featuring vigorous updrafts capable of lofting large amounts of supercooled liquid water, forming graupel and hail (Zipser, 2003). Furthermore, this region is known for supercells which form under strong vertical wind shear and can produce large hail, tornadoes, and damaging winds. At larger scales, convection frequently organizes into MCSs, especially nocturnal systems that form in association with the LLC (Carbone et al., 2002). It is anticipated that convection here tends to have lower precipitation efficiency compared to tropical systems. This is due to the stronger updrafts producing more graupel and hail, and the drier mid-levels promoting evaporation of rain before it reaches the surface. This contrasts with maritime systems, where weaker updrafts and more humid profiles favor warm-rain processes and higher precipitation efficiency.

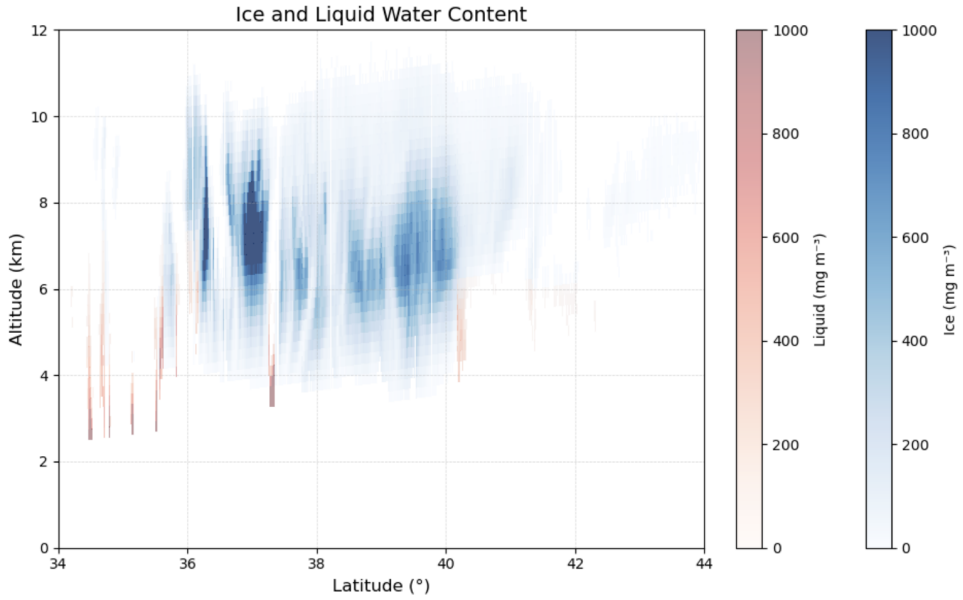

Figure 11: As in figure 7, regarding the September 29th, 2014 case over the Great Plains

The combined satellite products provide a detailed cross-sectional view of the microphysical and dynamical structure of the convective system (Fig. 10). The vertical wind shear profile (Fig. 12) shows weak lower-level shear (0.00 m s^{-1}), moderate midlevel shear (14.40 m s^{-1}), and comparatively weak upper-level shear (2.27 m s^{-1}), indicating that the strongest directional and speed shear is concentrated between 850–

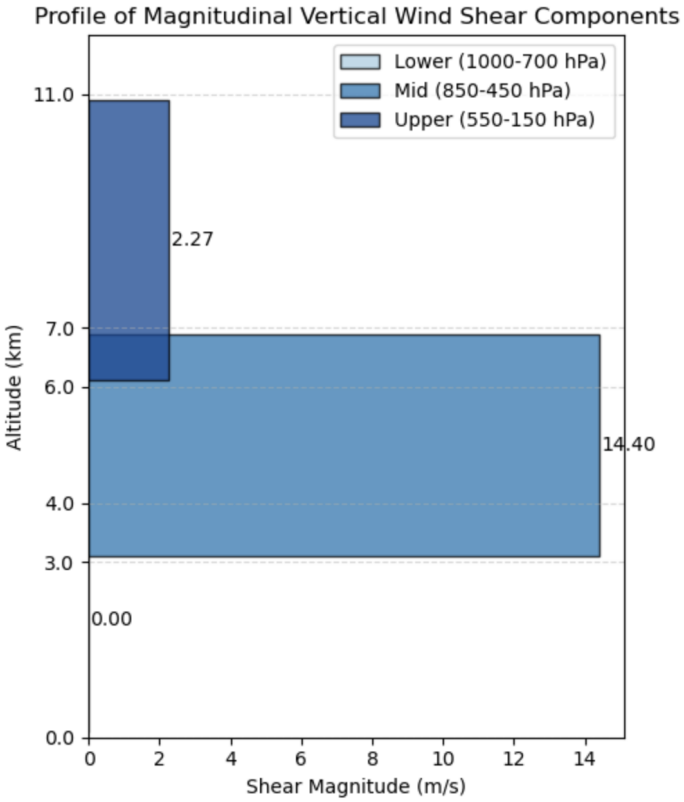

Figure 12: As in figure 5, regarding the September 29th, 2014 case over the Great Plains

450 hPa. This shear structure is consistent with a mature, forward-propagating MCS embedded within the South American Low-Level Jet regime, where midlevel shear contributes to storm organization and tilting of the convective cores. The hydrometeor cross section (Fig. 14) shows that liquid water content is primarily confined below 4–5 km, while ice water content dominates above this level and extends to roughly 11 km, with peak values clustered between 7–10 km. This vertical separation of liquid and ice is characteristic of deep continental convection with strong mixed-phase processes, where robust riming and aggregation occur in the upper portions of the storm.

Along-track ice water path exhibits several pronounced maxima (Fig. 13) that align with, but are broader than, the peaks in AMSR2 rain rate, indicating that extensive anvil and stratiform outflow regions are lofting and maintaining large quantities of ice even where surface rainfall is weak. The zonal-mean hydrometeor

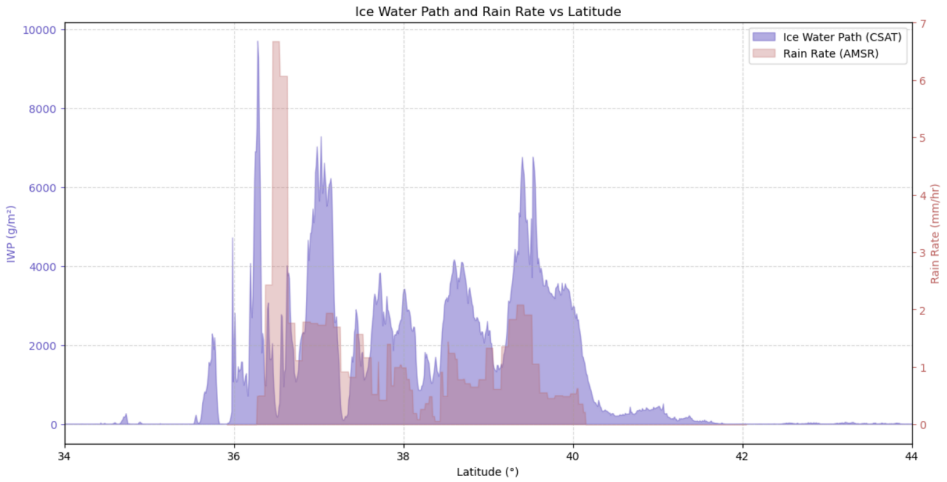

Figure 13: As in figure 6, regarding the September 29th, 2014 case over the Great Plains

profiles (Fig. 14) show a sharp decrease in liquid water above 6 km and a monotonic increase in ice water content with height, followed by a gradual decline near 11 km. This behavior suggests sustained upper-level ascent and continuous production of small ice particles feeding the anvil, with an eventual transition into a more stable layer near the tropopause where vertical motion weakens and ice residence time decreases.

The radiative structure of the system (Fig. 15) is dominated by strong shortwave cooling across both the convective cores and the anvil canopy, reflecting the optical thickness of the ice-rich outflow. Longwave warming is collocated with the deepest cloud tops, where cold, high-altitude anvils trap outgoing terrestrial radiation. The net cloud radiative effect remains negative over most of the transect, indicating that shortwave reflection by the extensive anvil outweighs longwave greenhouse effects. Only near the northern periphery of the system does the net CRE approach neutrality, corresponding to thinner cloud regions with reduced SW reflectance. Together, these profiles characterize a highly organized, ice-dominated convective system typical of the Argentinian convection hotspot, with strong midlevel shear, deep glaciation, and radiative impacts dominated by shortwave cooling from an extensive, optically thick anvil.

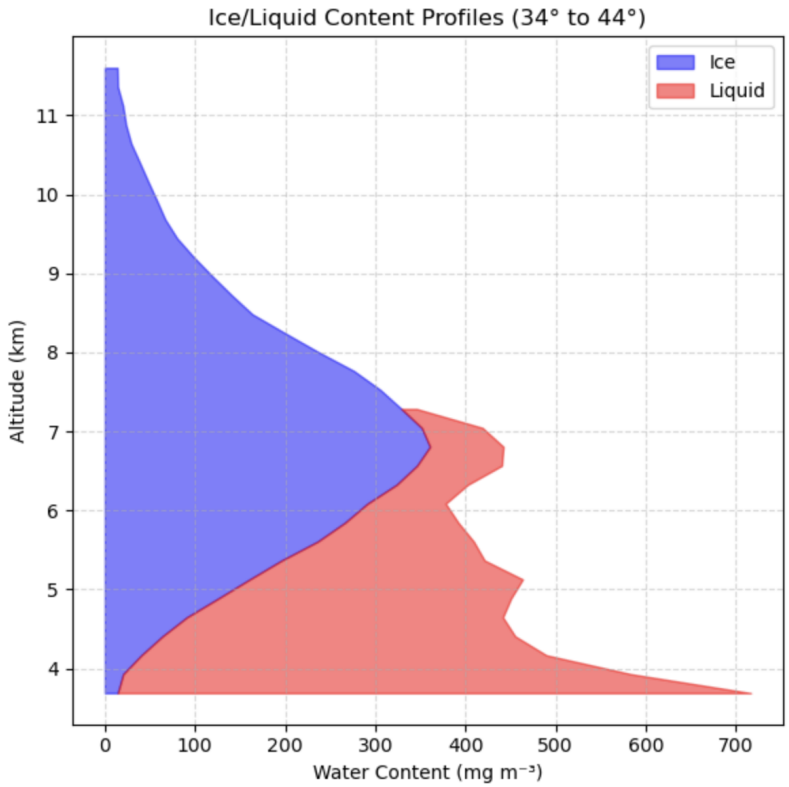

Figure 14: As in figure 8, regarding the September 29th, 2014 case over the Great Plains

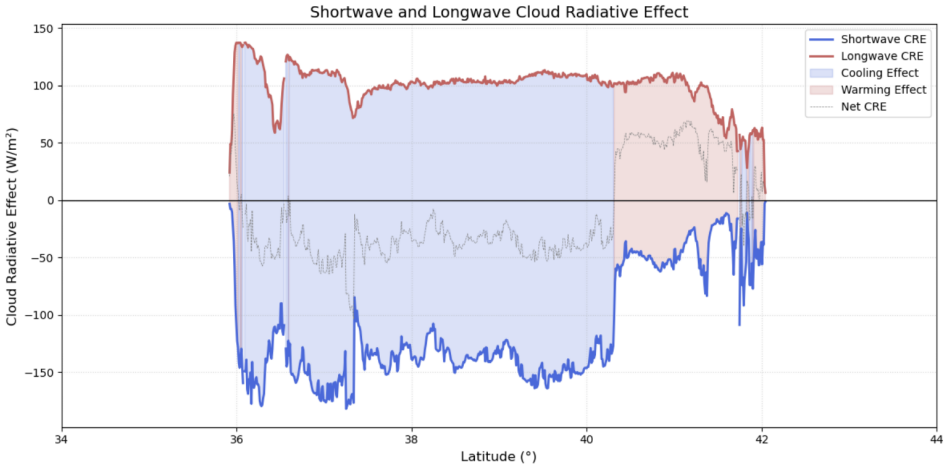

Figure 15: As in figure 9, regarding the September 29th, 2014 case over the Great Plains

3.2 Tropical Deep Convection

3.2.1 April 23rd, 2014: Western Coast of Africa

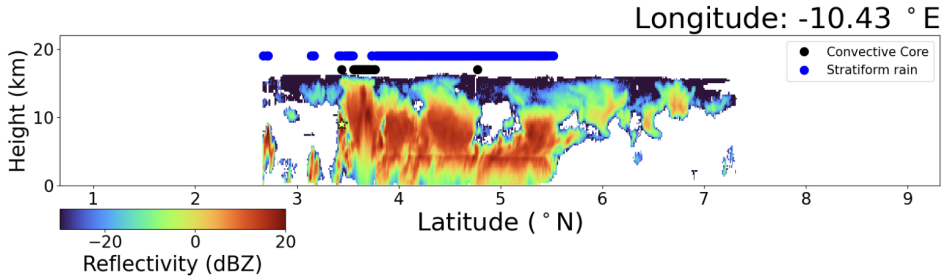

Figure 16: As in figure 4, regarding the April 23rd, 2014 case off the western coast of Africa

The western coast of Africa is a climatologically active region for convection due to a multitude of reasons, including warm sea surface temperatures, moisture influx from the ocean and land stemming from the West African Monsoon, and influence from the African Easterly Jet (AEJ). This combination of variables helps trigger MCSs that typically originate over land, and move westward over the ocean due to southeast and northeast trade winds, where they can maintain or enhance into deep oceanic convection (Wu et al. 2014).

However, new convection can also initiate offshore, especially in the evening or overnight due to land-sea breeze circulations SST diurnal cycles (Djakouré et al 2024). Oceanic convection near the coast often peaks at night, lagging behind continental convection which peaks in the late afternoon (Vizy and Cook 2017). This is due to to stabilization over land at night and continued instability over the warm ocean. These systems are known for reaching very high altitudes, producing large amounts of ice particles and cold cloud tops. This region also contributes to the moist static energy export into the Atlantic Intertropical Convergence Zone (ITCZ) and helps sustain the Atlantic Walker circulation.

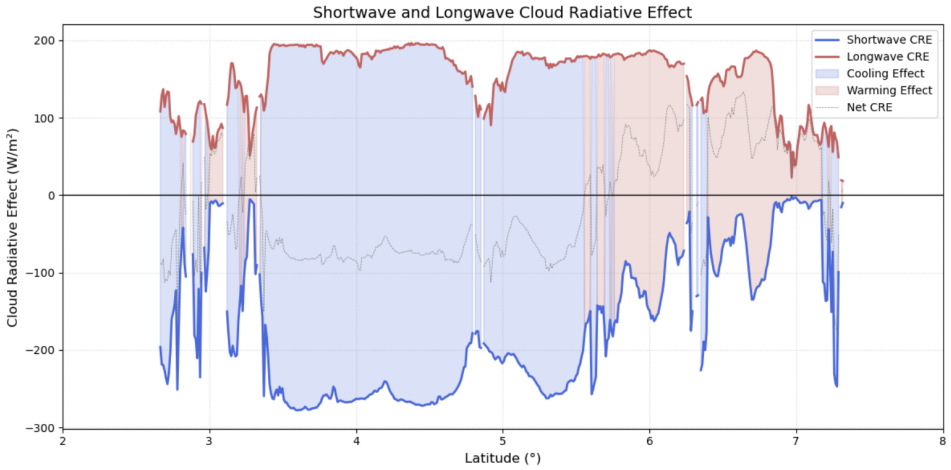

Figure 17: As in figure 9, regarding the April 23rd, 2014 case off the western coast of Africa

The most prominent idea about this event is not only how deep it extends into the atmosphere, reaching nearly 20 km, but also the radiative implications of it doing so (Fig. 17). Extraordinarily deep convection, and subsequent high anvil clouds, make the radiative impacts even more pronounced. Due to the depth of this system, it can be inferred that the system is optically thick with a very high albedo, reflecting a large portion of solar radiation. As seen in Figure 17, SW CRE becomes very negative, greatly exceeding $-200\ \mathrm{W\,m^{-2}}$, causing the underlying ocean to receive significantly less solar energy, contributing to cooling which can in turn feed back on local convection. Coupled with this, strong positive LW CRE is occurring, where contrastingly the atmosphere below the cloud is warmed because outgoing radiation is being "trapped". Oftentimes, it appears that the SW CRE is the dominant contributor to the radiative impact of this system, and that areas of cooling are in areas of the highest reflectivity. The switch to a net warming cloud occurs as

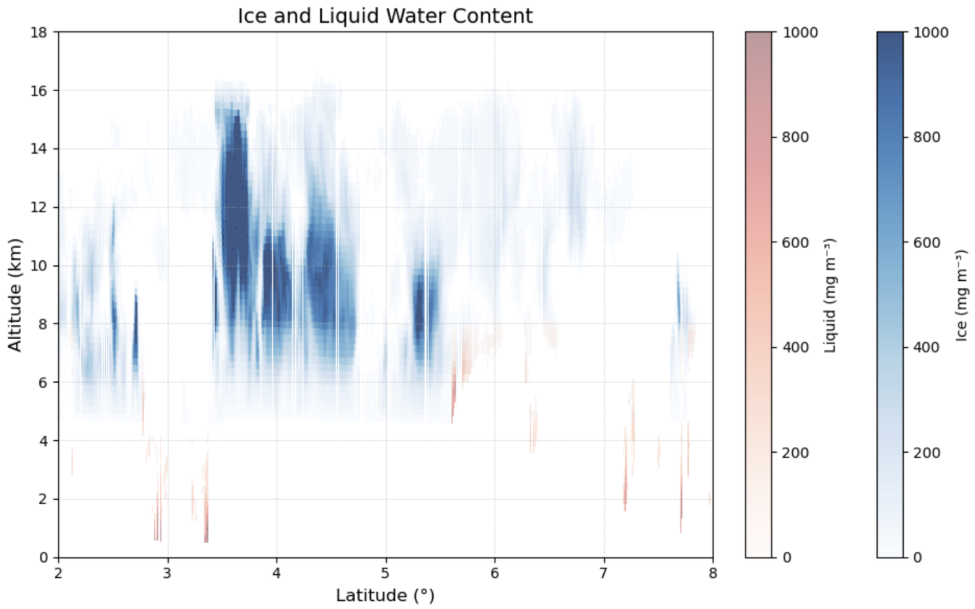

Figure 18: As in figure 7, regarding the April 23rd, 2014 case off the western coast of Africa

the vertical structure of the cloud turns from the main cloud system to what could be a trailing anvil. Anvils generated by tall convection can persist for several hours, and can sustain these radiative effects long after deep convection subsides. The broader implications of cloud tops at this height is that overshooting tops can inject water vapor and ice into the lower stratosphere further affecting radiative forcing and stratospheric chemistry.

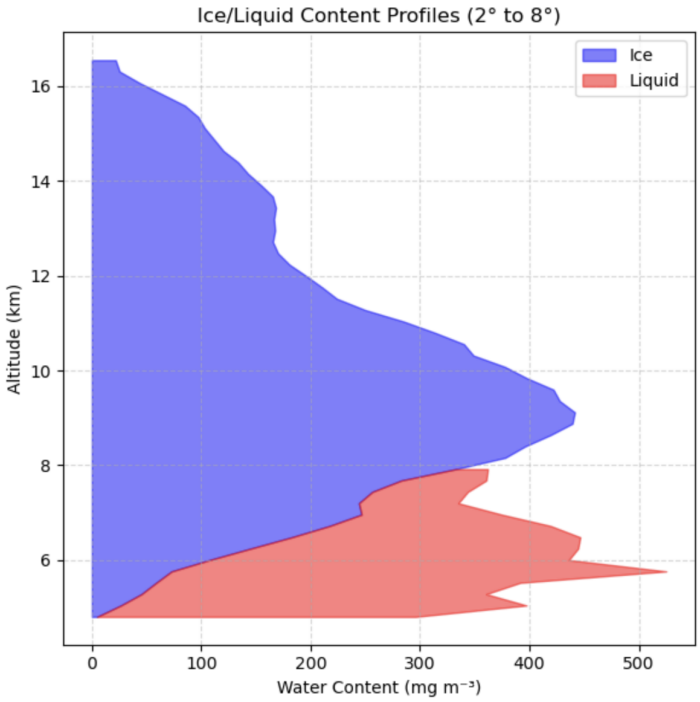

Figure 19: As in figure 8, regarding the April 23rd, 2014 case off the western coast of Africa

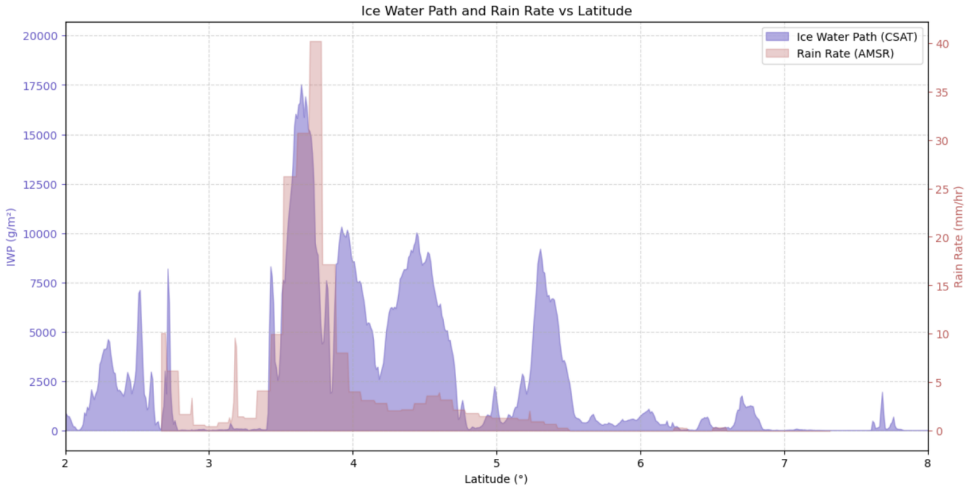

Figure 20: As in figure 6, regarding the April 23rd, 2014 case off the western coast of Africa

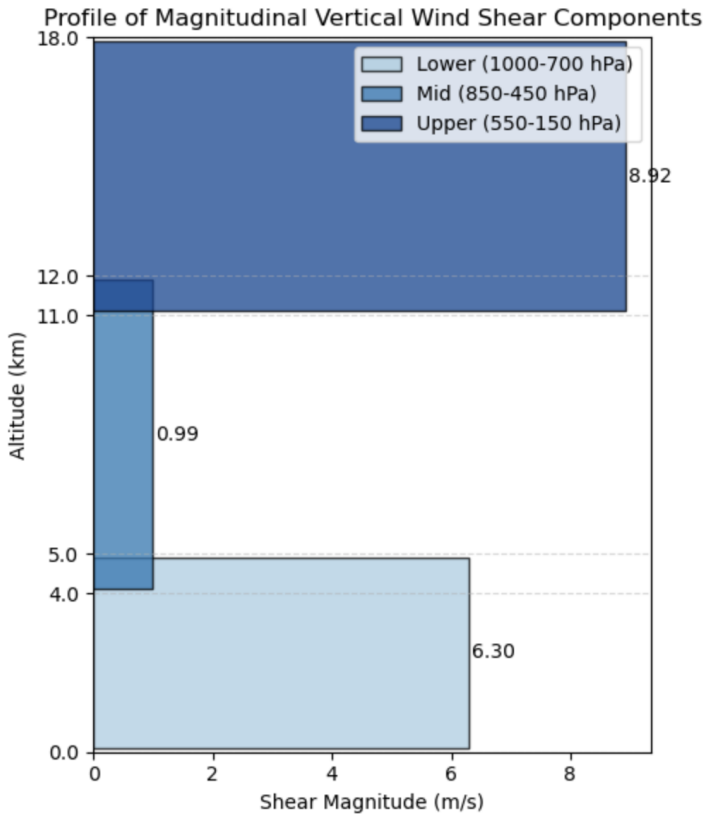

Figure 21: As in figure 5, regarding the April 23rd, 2014 case off the western coast of Africa

The shear (Fig. 21) for this convective event is quite low compared to earlier analyzed case studies, but this is to be expected with being so close to the equator, where Coriolis force is near its lowest values. This is due to Earth's rotation, and the subsequent Coriolis-driven balance between pressure gradients and wind breaks down as Coriolis approaches zero at lower latitudes. Therefore other areas in the world usually have zonal and meridional winds, where the tropics around the equator mostly zonal winds that are often uniform with height. Such a low vertical shear disallows any tilting of the updraft, which gives the characteristics of upright, deep vertically stacked clouds, with less horizontal organization.

3.2.2 April 30th, 2016: The Maritime Continent

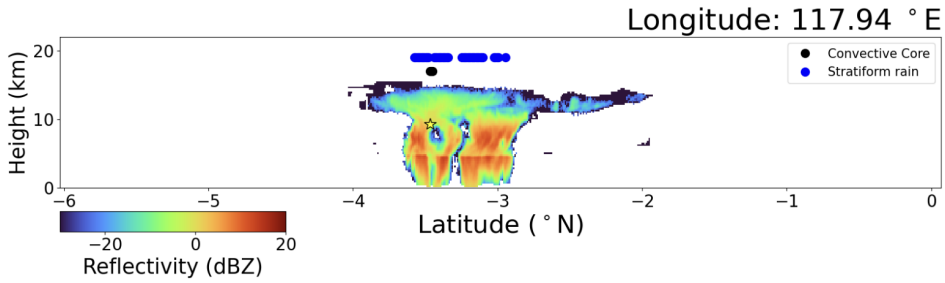

Figure 22: As in figure 4, regarding the April 30th, 2016 case, over the Maritime Continent

The maritime continent has some of the most persistent convection on the planet, and plays a major role in global circulation. This region overlies the warmest sea surface temperatures globally, often exceeding 29 degrees C, which proves abundant surface heat and moisture fluxes (Ramage, 1968; Neale and Slingo, 2003). Combined with a moist troposphere, these conditions sustain convective towers that frequently reach the upper troposphere (Houze et al. 1981). A defining feature of maritime continent convection is its strong diurnal cycle, driven by land/sea interactions. Over large isalnds such as Sumatra, Borneo, and New Guinea, strong daytime solar heating produces vigourous updrafts that fuel deep convection (Qian, Robertson, and Moron, 2010). At night, offshore convergence from land breezes triggers deep convection over adjacent seas (Yang and Slingo, 2001). Deep convection here often organizes into MCSs consisting of convective cores with heavy rainfall and graupel aloft, surrounded by broad stratiform rian regions and extensive cirrus anvils (Houze, 1989; Nesbitt, Zipser, and Cecil 2000). These anvils exert strong radiative impacts by reflecting solar radiation while trapping outgoing long wave fluxes. Deep convection over the maritime continent plays a central role in the global hydrological cycle and atmospheric circulation, releasing large amounts of latent heat into the upper troposphere and acting as a key driver of the Hadley and Walker circulations (Houze 2018).

Deep convection in the maritime continent is also notable for its large ice water content aloft, which plays a central role in both precipitation processes and radiative effects. Strong updrafts frequently loft supercooled liquid water and ice particles to the upper troposphere, where they contribute to the development of broad

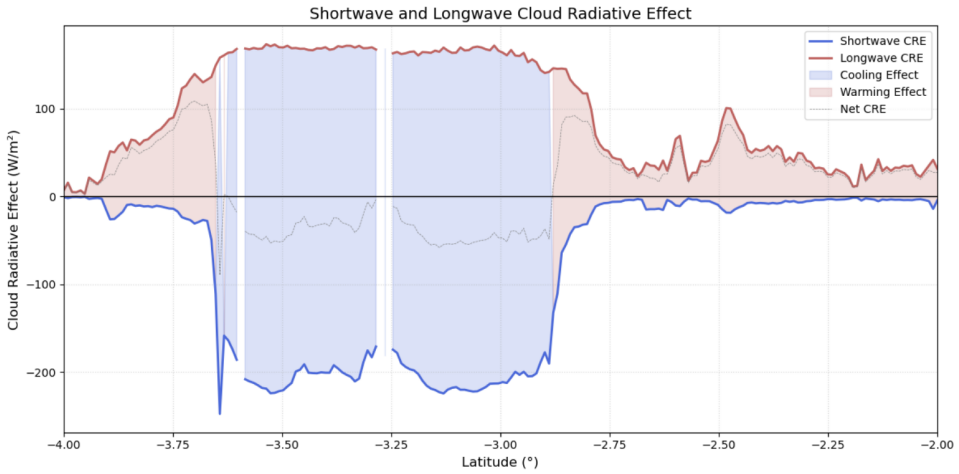

Figure 23: As in figure 9, regarding the April 30th, 2016 case, over the Maritime Continent

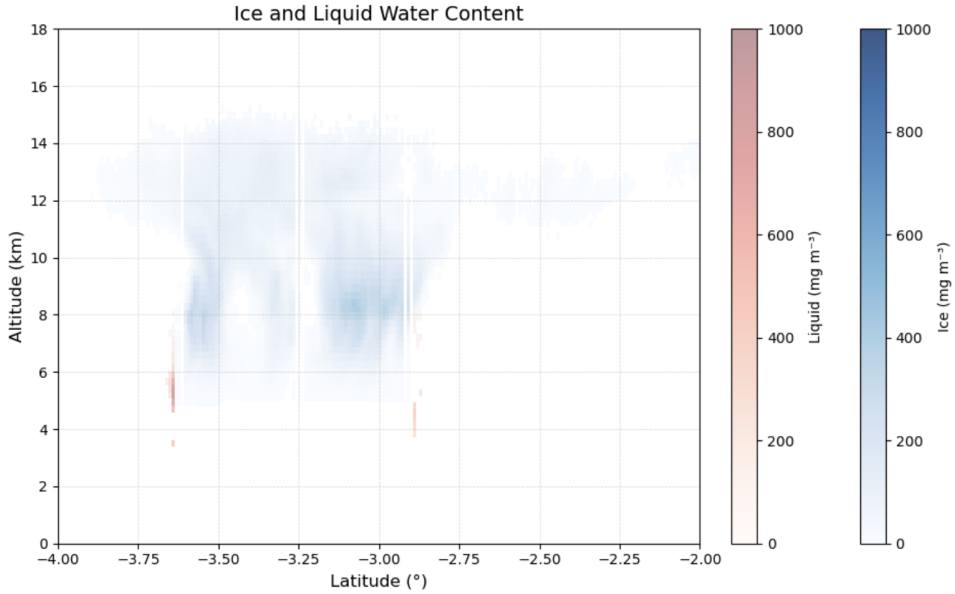

Figure 24: As in figure 7, regarding the April 30th, 2016 case, over the Maritime Continent

cirrus anvils and stratiform cloud decks (Zipser, 2003; Houze, 2018). Compared to continental convection, maritime systems often exhibit somewhat lower peak updraft velocities, but the high moisture availability over warm waters enables sustained ice mass flux into the upper troposphere. The distribution of ice particle

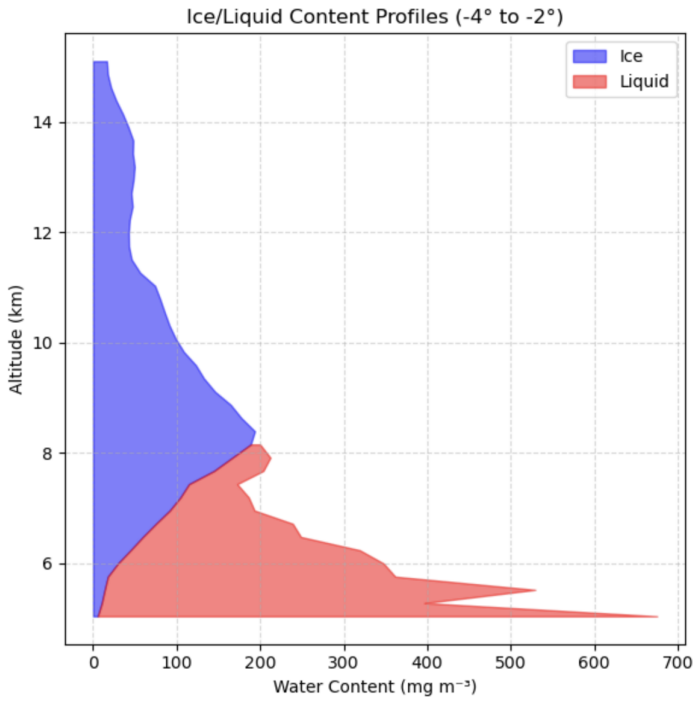

Figure 25: As in figure 8, regarding the April 30th, 2016 case, over the Maritime Continent

sizes is critical, where large particles sediment rapidly, enhancing precipitation efficiency. Smaller ice crystals are more likely to persist aloft, increasing cloud longevity and subsequent radiative forcing. Observations from CloudSat indicate that MCSs in this region produce extensive upper-level ice clouds, with IWC magnitudes sufficient to modulate both shortwave reflection and longwave trapping on regional to global scales (Gayat et al. 2014). Thus, the vertical transport and microphysical partitioning of ice in maritime continent convection directly shape its dual role in the hydrological cycle and Earth's radiation budget.

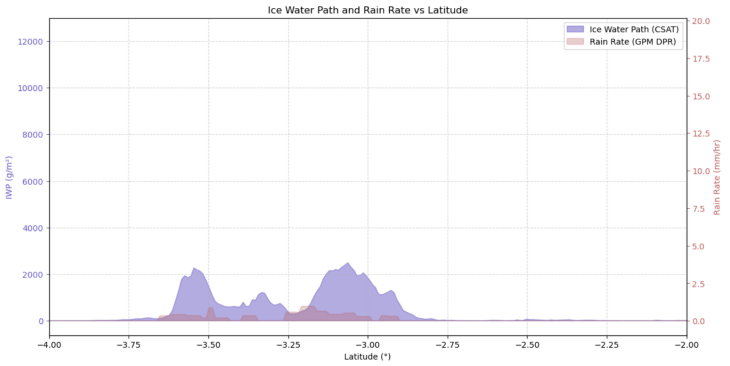

Figure 26: As in figure 6, regarding the April 30th, 2016 case, over the Maritime Continent

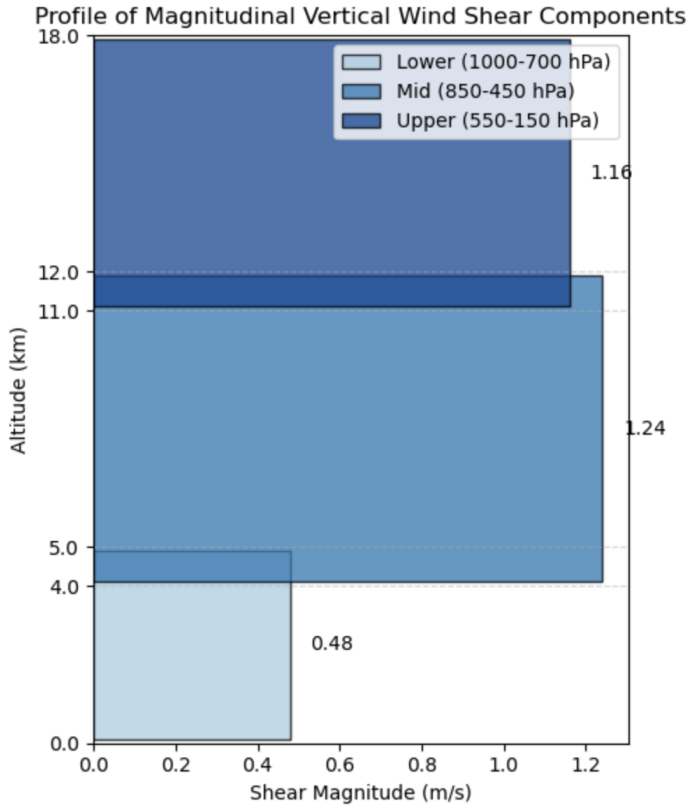

Figure 27: As in figure 5, regarding the April 30th, 2016 case, over the Maritime Continent

The vertical cross section (Fig. 22) of CloudSat reflectivity illustrates a deeply developed convective system characteristic of the Maritime Continent, with multiple convective towers embedded within a broad anvil canopy extending to approximately 15–16 km. Reflectivity exceeding 20 dBZ in the midlevels indicates substantial ice mass aloft, while the relatively weak near-surface reflectivity suggests limited conversion of condensate to surface rainfall along the CloudSat track. This vertical structure is consistent with strongly ventilated tropical convection in regions of moderate-to-strong shear. The cloud radiative effect fields (Fig. 23) show pronounced shortwave cooling within the convective region, reaching values below -200 W m^{-2}, while the longwave component contributes a substantial warming of over 150 W m^{-2}, typical of thick, cold-topped anvil clouds. The net CRE remains dominated by shortwave cooling over the core of the system, transitioning to weak warming on the periphery. Hydrometeor profiles indicate a deep layer of ice extending above 14 km, with liquid water primarily confined below 8 km, consistent with strong upper-level detrainment and vigorous mixed-phase microphysics. The along-track IWP exhibits large peaks exceeding 2000 g m^{-2} within the convective cores, while corresponding GPM DPR rain rates remain comparatively small (Fig. 26), further supporting the interpretation of inefficient precipitation processes common in sheared, strongly ventilated tropical systems. Vertical shear profiles show weak lower-tropospheric shear, (Fig. 27) stronger midlevel shear (850–450 hPa), and sustained upper-level shear through 150 hPa, a configuration conducive to deep, long-lived convective systems with broad anvil production. Collectively, these structural, radiative, and microphysical characteristics are consistent with robust mesoscale convective organization frequently observed over the Maritime Continent, where complex interactions among thermodynamics, moisture convergence, and vertical shear promote intense ice production and strong radiative impacts.

3.3 Tropical Deep Convection - Walker Circulation Main Branches

The following cases occur within regions strongly influenced by the ascending and descending branches of the Walker circulation. The Walker circulation is the zonal overturning cell of the tropical Pacific, maintained by the contrast between warm western Pacific sea surface temperatures (SSTs), which support vigorous deep convection, and the cooler eastern Pacific cold tongue, where subsidence dominates. This zonal SST gradient drives low-level easterlies that converge over the warm pool, ascend in deep convective towers, and return eastward aloft before sinking over the cooler basin, as shown in Figure 28(Power and Smith 2007; Hosking

et al 2012).

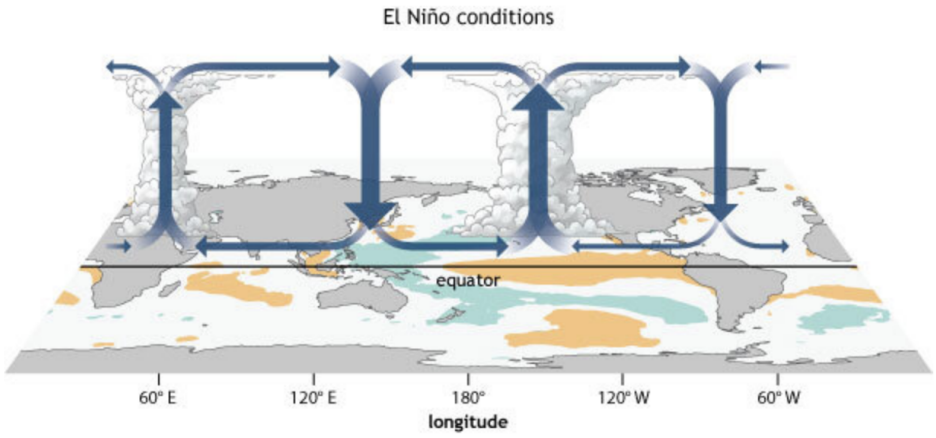

Figure 28: Graphic taken from NOAA's climate.gov, illustrating the general behavior of the Walker Circulation during El Niño conditions.

During El Niño events, however, the SST gradient weakens and warm anomalies extend into the central and eastern Pacific. Deep convection shifts eastward, altering the location of the main rising branch and weakening the subsidence over the eastern Pacific. This reorganization of convection and large-scale vertical motion modulates the environments sampled in the following case studies, particularly those occurring in regions influenced by the anomalous El Niño Walker pattern (Yun et al. 2021).

3.3.1 October 7th, 2015: The Eastern Pacific Ocean

This deep convective system is located off the southwest coast of Mexico, directly west of Nicaragua. This is an area known for deep convection, especially during boreal summer and early fall. It is part of the Pacific ITCZ, and lies near the main region of ascent in the walker circulation. Convective systems here often reach the upper troposphere, and can produce expansive cold shields. They frequently organize into mesoscale convective systems within the ITCZ band, and due to similar reasons already discussed due to proximity to the equator limiting vertical wind shear and having high moisture content, convection is often vertically deep and upright, supporting strong latent heat release. This region is an important area of study due to its

critical role in maintaining the energy and moisture balance of the eastern tropical Pacific, as well as the seeds these systems sow in regards to tropical cyclone formation, particularly during the Eastern Pacific hurricane season. Furthermore, through latent heat release, deep convection in this region contributes to upper-level divergence and can influence Rossby wave propagation and downstream weather patterns, including over North America (Huaman et al. 2020). Vertical profiles often show strong radar reflectivity cores in the lower and mid-troposphere, capped by high-altitude ice-rich anvils that strongly affect outgoing longwave radiation.

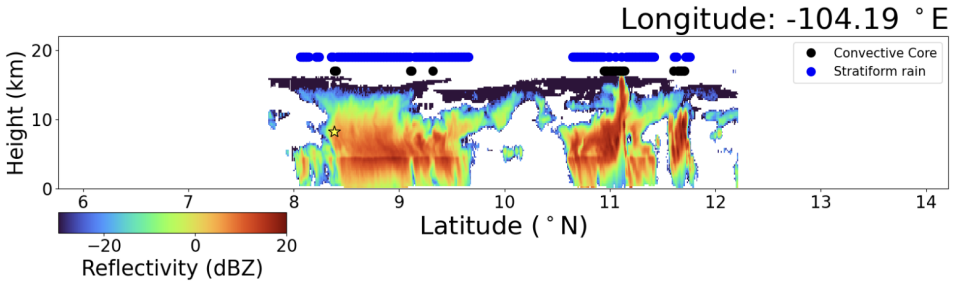

Figure 29: As in figure 4, regarding the October 7th, 2015 case, over the Eastern Pacific

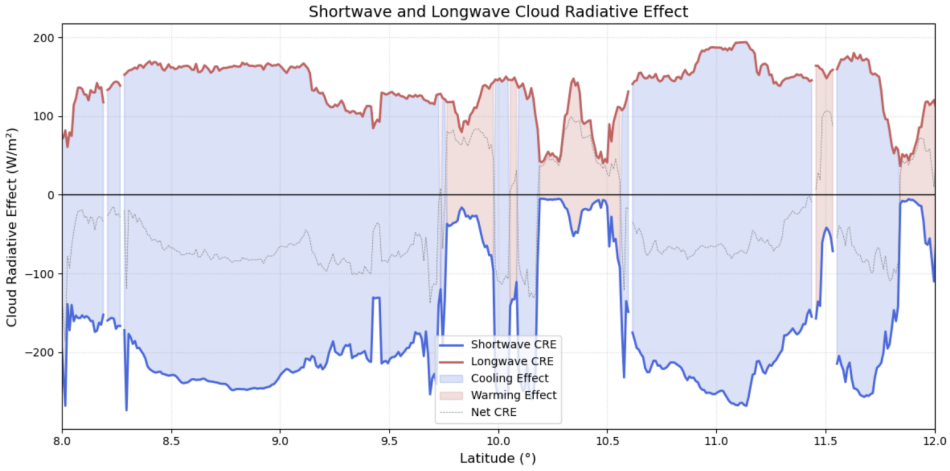

Figure 30: As in figure 9, regarding the October 7th, 2015 case, over the Eastern Pacific

The vertical structure of this case extends upwards of 18 km with multiple convective cores (Fig. 29) and high reflectivity values throughout the system. The radiative implications show a general trend of

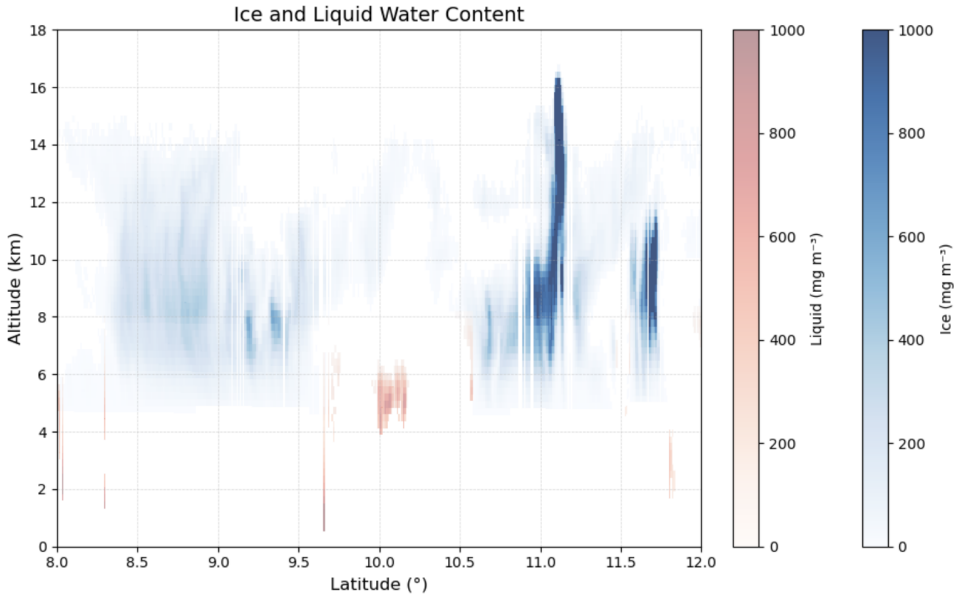

Figure 31: As in figure 7, regarding the October 7th, 2015 case, over the Eastern Pacific

cooling in instances of high reflectivity where hydrometeors extend to the surface, and warming where there are suspended hydrometeors (Fig. 30), aligning with the trends seen in cases both in the tropics and midlatitudes analyzed above. This case is accompanied with moderate to high levels of shear (Fig. 34), the most prominent being in the midlevel.

The cloud and precipitation structure observed between 8° and 12°N off the southwest coast of Mexico reveals a coherent deep convective system embedded within the eastern Pacific sector of the Walker circulation during an El Niño year. The cloud radiative effects exhibit strong latitudinal variability (Fig. 30), with shortwave cooling exceeding -200 W m^{-2} in several bands and longwave warming reaching 100–200 W m^{-2}. Regions of enhanced LW CRE, particularly between 10.8° and 11.3°N, coincide with strong convective features identified in the hydrometeor fields. Vertical profiles (Fig. 32) of cloud water content averaged over the transect show a deep ice layer extending from approximately 8 km to 17 km, with maximal IWC between 12 and 15 km, while liquid water content is confined to 5–8 km with peaks near 6–7 km. These structures indicate mature deep convection with well-developed glaciated anvils.

Latitudinal variations in hydrometeor loading further support this interpretation: the IWP exhibits pro-

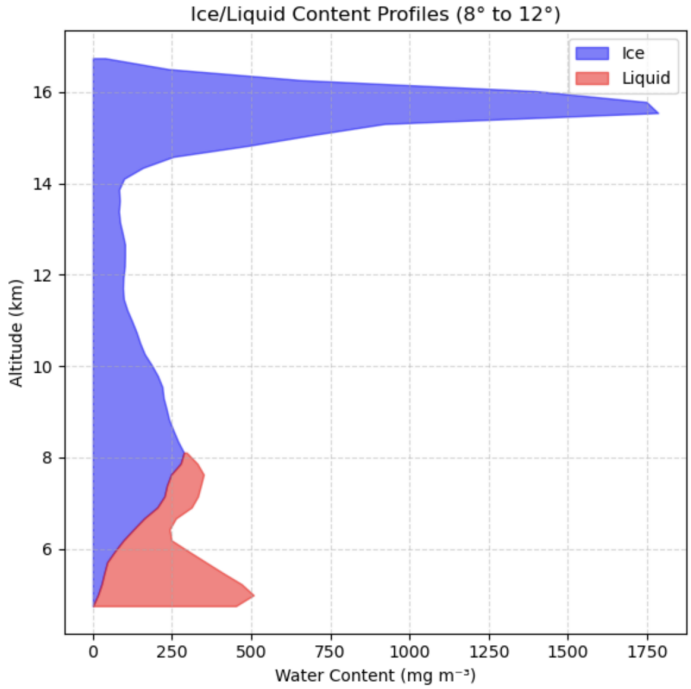

Figure 32: As in figure 8, regarding the October 7th, 2015 case, over the Eastern Pacific

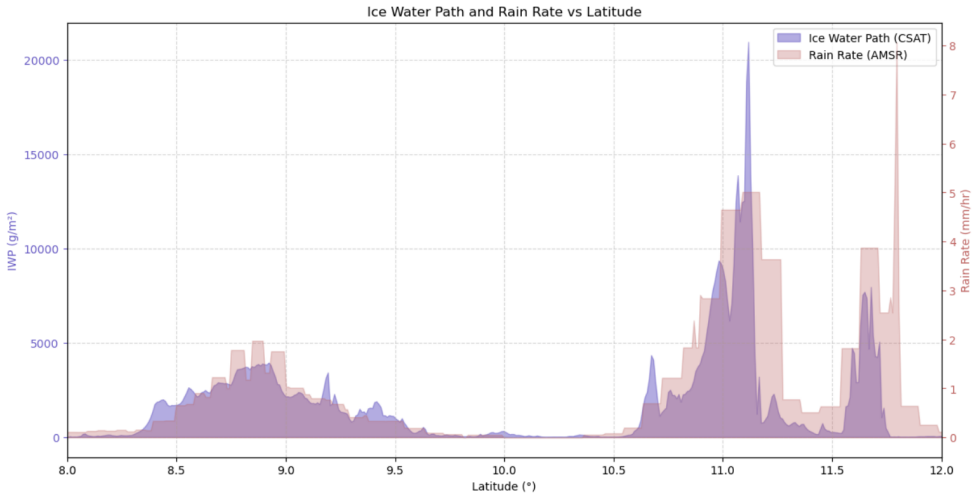

Figure 33: As in figure 6, regarding the October 7th, 2015 case, over the Eastern Pacific

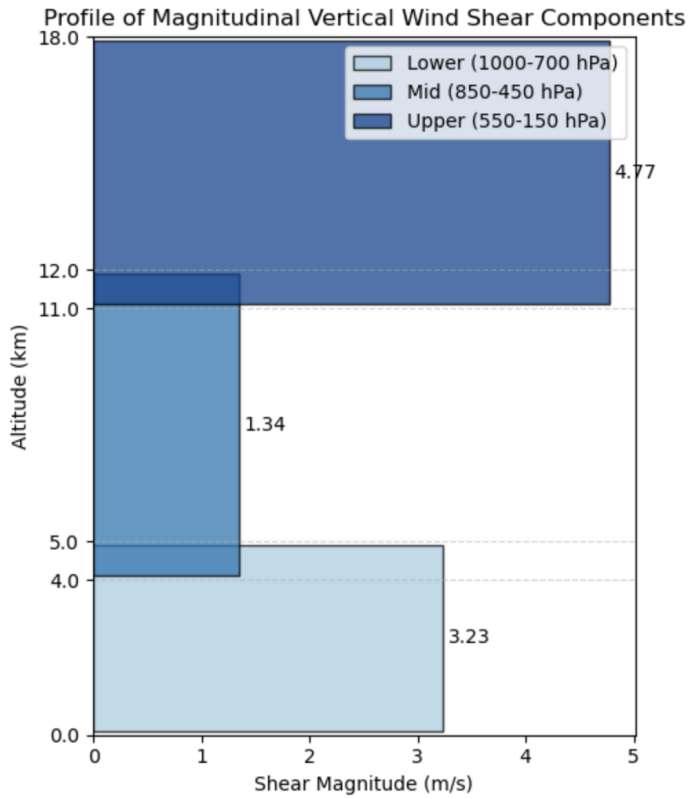

Figure 34: As in figure 5, regarding the October 7th, 2015 case, over the Eastern Pacific

nounced maxima near 8.3°, 9°, and 10.8–11.3°N, each colocated with increases in AMSR2 rain rate (Fig. 33). The strongest precipitation and deepest ice columns occur between 10.8° and 11.5°N, consistent with the deepest convective towers visible in the vertical curtain plot. Liquid water maxima below 7 km align with these cores, indicating active warm-rain processes transitioning into substantial upper-tropospheric glaciation. Environmental wind shear profiles show moderate low-level shear (3.2 m s^{-1}), weak mid-level shear (1.3 m s^{-1}), and strong upper-level shear (4.8 m s^{-1}), a structure that favors the formation and horizontal spreading of extensive anvil clouds. Collectively, the radiative signatures, hydrometeor distributions, precipitation patterns, and shear environment are consistent with organized deep convection characteristic of the climatological adjustments expected during El Niño, when the Walker circulation's ascending branch shifts eastward and supports enhanced convective activity in this region.

3.3.2 October 9th, 2015: The Western Pacific Ocean

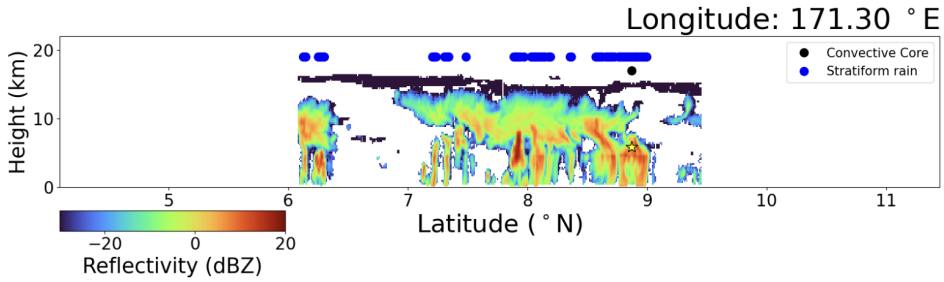

Figure 35: As in figure 4, regarding the October 9th, 2015 case, over the Western Pacific

This case is an oceanic case located to the northeast of Papua New Guinea, in the Western Pacific Warm Pool and near the main rising branch of the Walker cell due to the warm SSTs and strong moisture convergence. The Western Pacific Warm Pool is characterized by some of the warmest SSTs on the planet, often exceeding 29-30C year round. These persistently warm SSTs drive intense surface evaporation, creating a highly moist boundary layer and fueling the strong convective instability needed for frequent and sustained deep convection. The region is also near the main descending branch of the Walker circulation, which further enhances vertical motion through large-scale moisture convergence and low-level easterly trade winds that accumulate warm, moist air from across the Pacific. Convection in this area is often vertically deep and highly organized, with cloud tops regularly reaching the tropical tropopause and forming expansive anvil clouds composed primarily of ice. These systems contribute significantly to latent heat release, which reinforces upper-level divergence and supports broader atmospheric circulations, including Hadley and Wlaker cells. Because of the favorable thermodynamic environment, the region supports not only frequent isolated convection, but also the development of mesoscale convective systems and organized tropical disturbances. This area is also notable for its role in cloud-radiation interactions. High, optically thick anvil clouds generated by deep convection significantly impact the Earth's radiation budget, especially by reducing outgoing longwave radiation and increasing shortwave reflectiveness. These radiative effects are globally significant because of the perissitent nature of convection in the wamr pool and the spatial extent of the resulting cirrus anvils. Importantly, this region is also sensitive to ENSO variability. During El Nino, the center of maximum

convection may shift eastward into the central Pacific, weakening convection over the warm pool. During La Nina, this region becomes even more convectively active, with intensified rainfall and stronger Walker circulation ascent.

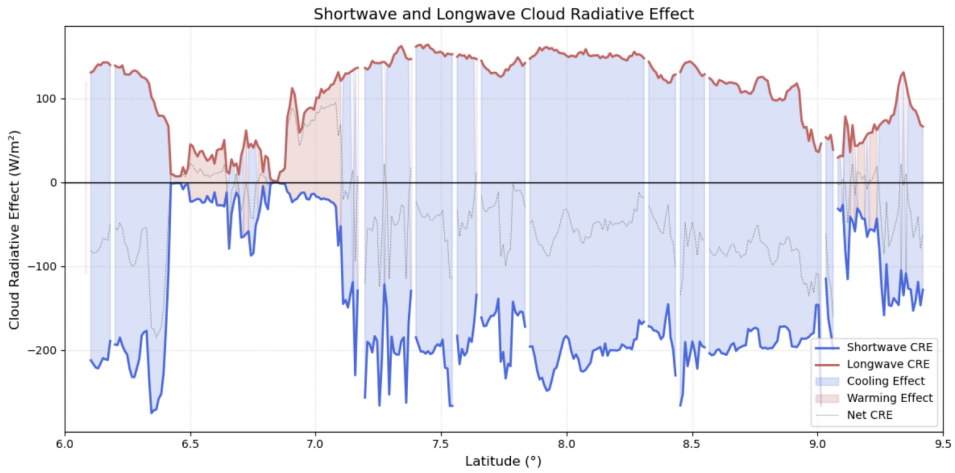

Figure 36: As in figure 9, regarding the October 9th, 2015 case, over the Western Pacific

The more noticeable thing about this instance of deep convection is that the vertical and spatial structure of the system is greatly disorganized (Fig. 35), with an undefined core despite the depth and intensity of the storm. It appears the greater system is composed of highly stacked convective towers that extend high into the atmosphere, having extremely cold brightness temperatures, yet there is heavy fall-out from solid precipitation. Despite the small spatial scale these clusters of convective cores take, there appears to be a mostly cooling effect in regions of the core, and warming in regions of an upper anvil. Although shear is low to moderate (Fig. 40), it is possible the existence of an anvil occurs due to the upper level shear being slightly greater than levels closer to the surface.

Taken together, the Case 5 (October 7th, 2015) and Case 6 (October 9th, 2015) events illustrate the contrasting convective structures and environmental controls associated with the ascending versus descending branches of the Walker circulation during El Niño conditions. Case 5, located within the eastward-shifted ascending branch, exhibits a highly organized mesoscale convective system with multiple coherent convective cores, strong hydrometeor loading, and deep, glaciated anvils extending to 17–18 km. Its CRE signatures

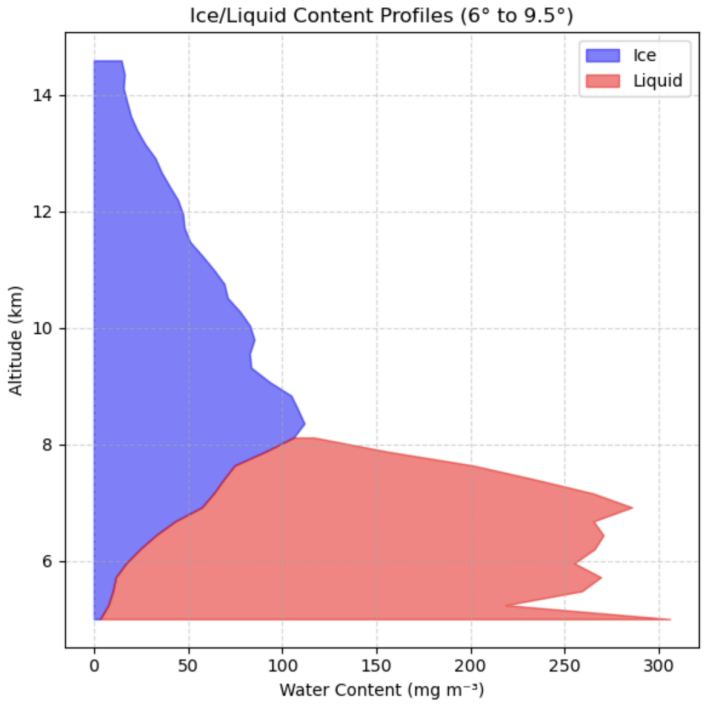

Figure 37: As in figure 8, regarding the October 9th, 2015 case, over the Western Pacific

show strong shortwave cooling and pronounced longwave warming colocated with deep convective towers, consistent with vigorous latent heating and robust upper-level divergence. Hydrometeor fields reveal well-structured IWC maxima between 12 and 15 km and aligned LWC peaks below 7 km, producing clear stratification between warm-rain processes and upper-tropospheric glaciation. Moderate upper-level shear further promotes extensive anvil spreading, reinforcing the radiative impact of the system.

By contrast, Case 6 in the western Pacific warm pool displays a markedly more disorganized system despite occurring in a thermodynamically favorable environment with extremely warm SSTs and abundant column moisture. The vertical reflectivity and hydrometeor profiles reveal vertically stacked but spatially fragmented convective towers, lacking the cohesive convective line or well-defined core observed in Case 5. Ice water content remains deep but irregular, and the precipitation field shows localized heavy solid hydrometeor fallout embedded within broader, weakly stratiform regions. CRE patterns are correspondingly noisier, with pockets of strong cooling near embedded convective bursts and intermittent longwave warming under the

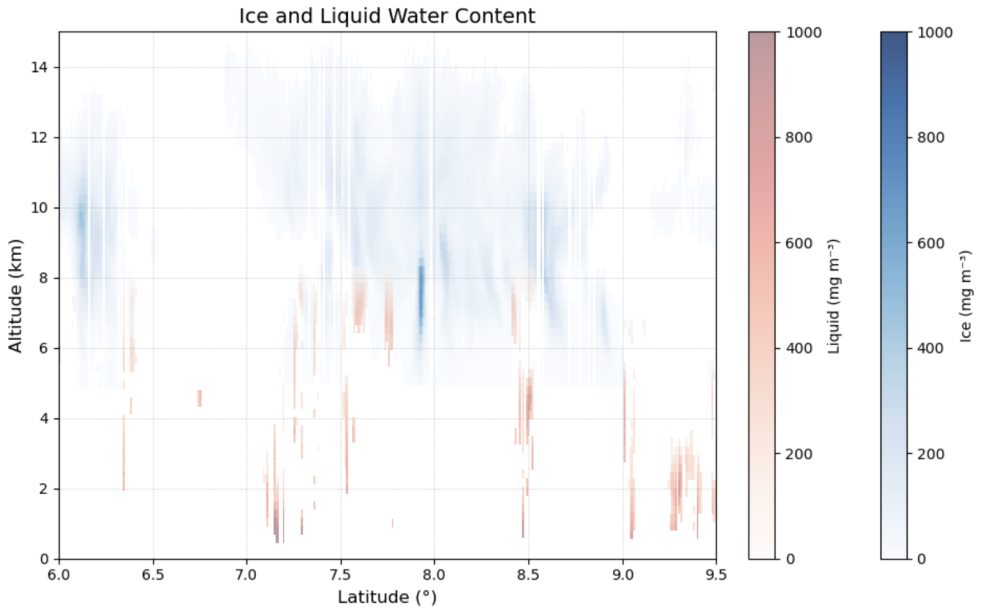

Figure 38: As in figure 7, regarding the October 9th, 2015 case, over the Western Pacific

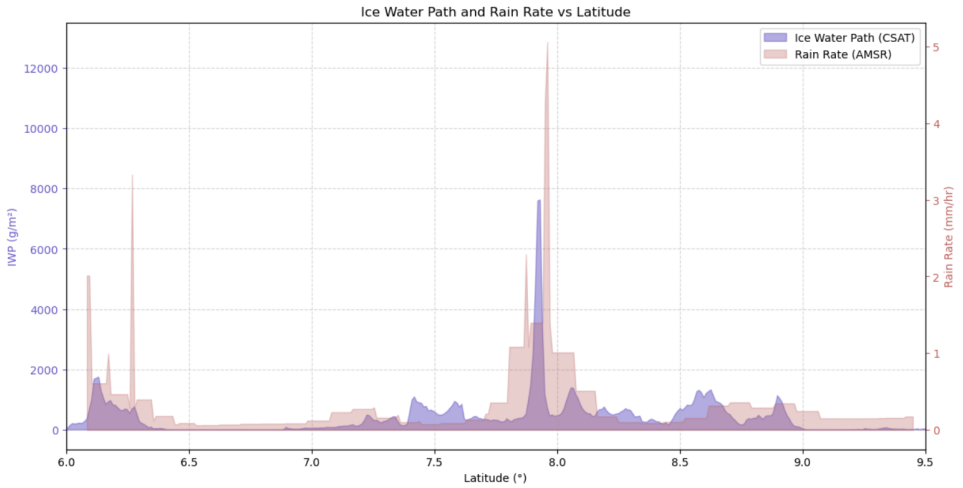

Figure 39: As in figure 6, regarding the October 9th, 2015 case, over the Western Pacific

diffuse anvil canopy. The weak low- and mid-level shear in this region appears insufficient to promote structural organization, while slightly enhanced upper-level shear allows only limited anvil development compared to Case 5.

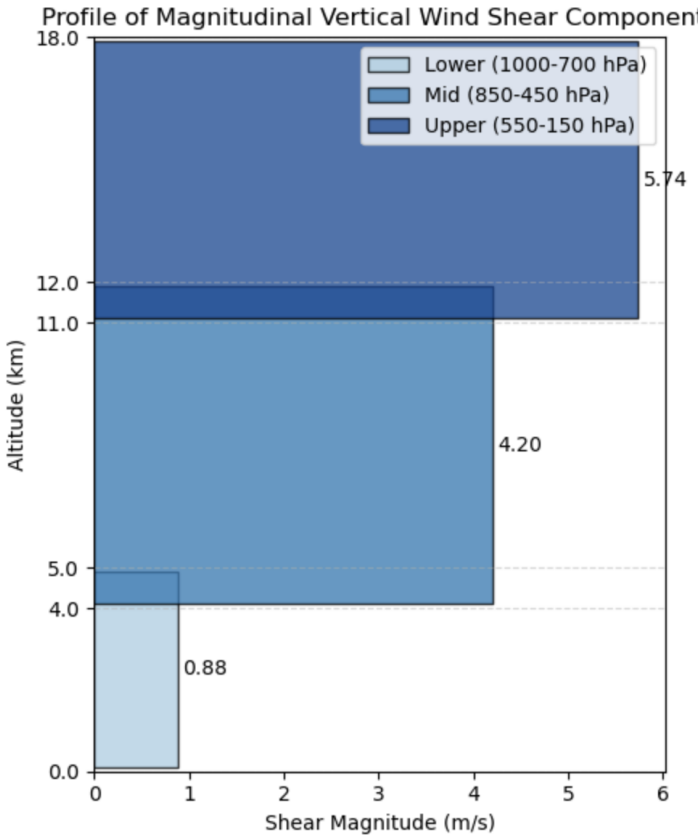

Figure 40: As in figure 5, regarding the October 9th, 2015 case, over the Western Pacific

These differences are consistent with the large-scale dynamical environment: Case 5 lies directly beneath the anomalously strengthened ascending branch of the Walker circulation during El Niño, which favors sustained deep convection, organized mesoscale structure, and strong radiative signatures. Case 6, despite its warm-pool location, resides nearer the weakened descending branch during El Niño, resulting in more disorganized convection, reduced vertical coherence, and more spatially heterogeneous radiative and microphysical characteristics.

4 Precipitation Efficiency Globally

4.1 Latitudinal Variations

Results thus far have been focused on individual cases and the environments surrounding them. However, the main purpose of this study is to be able to conduct analysis on general trends in PE over multiple different regions across the globe. Each case study was chosen from a regional box, as depicted in figure 3, but all figures in this section will be referencing averages across each regional box.

As expected, precipitation efficiency across each one of these boxes shows a clear distinction between the midlatitudes and the tropics. This is especially important considering the tropical regional boxes are a mix of maritime and land convection, and yet show minimal variance compared to one another. This could mean that land/sea distinction have less of an impact on PE than latitudinal changes, thus validating this research and the lack of land and ocean convection differentiation. Likewise, it also prompts further research to analyze additional regions to separate land-ocean convection from potential latitude effects. Breaking down the PE into its individual components provides a useful perspective on which terms in the PE equation are most influential (Fig. 41). This allows us to identify whether RR, LWP, or IWP exerts the strongest control on PE within each regional box. The figure illustrates a clear contrast between the midlatitude and tropical boxes, with values in the tropics being substantially larger across all variables. There is also a modest distinction between the two midlatitude regions: region 2 generally exhibits larger magnitudes than region 1 for most variables, except for LWP, where the two are nearly identical. This is particularly interesting given that the final PE values for the two midlatitude cases are quite similar, despite notable differences in the underlying components, especially IWP.

This contrast becomes even more apparent when decomposing PE into its ratioed liquid and ice components (RR/LWP and RR/IWP), shown in Figure 4. These ratios represent the efficiency with which liquid and ice water are converted into precipitation. Consistent with the earlier breakdown, all tropical cases cluster closely together, indicating remarkably similar behavior independent of land–ocean differences. In contrast, the midlatitude cases span the range of efficiencies, containing both the highest and lowest values. Notably, the RR/IWP ratios in Case 1 and Case 2 are nearly identical, yet their RR/LWP efficiencies dif-

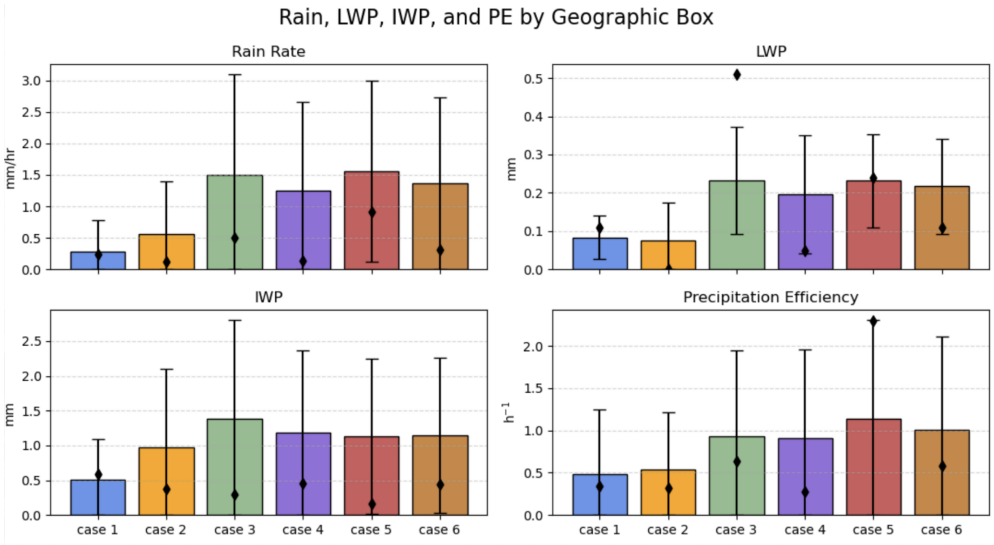

Figure 41: Rain rate, liquid water path, ice water path, and precipitation efficiency values for each regional box associated with each case study. Black bars represent normalized error, and black dots are associated with the individual values of each case study assocated with each given region

fer by more than a factor of two. This divergence suggests that liquid-phase processes distinguish the two midlatitude environments, while their ice-phase efficiencies remain comparable. Interestingly, Case 2 aligns more closely with the deep convective tropical cases than with Case 1, hinting that its environmental conditions share similar, though not identical, thermodynamic and microphysical characteristics with tropical convection.

A plausible physical explanation for the contrast between the two midlatitude regions is that the Argentina cases were sampled at an earlier stage of the convective lifecycle due to the timing of the CloudSat overpasses. Convection in northern Argentina often initiates in the late afternoon or early evening but does not typically reach its peak organization and stratiform expansion until several hours after initiation, frequently maturing late at night or in the early morning. Because CloudSat's local overpass time in this region occurs during or shortly after storm initiation, the satellite tends to observe these systems when updrafts are still developing, warm-rain processes are not yet fully established, and mesoscale organization has not yet emerged. In contrast, Great Plains convection could be sampled closer to its mature phase, when robust cold pools, deep stratiform regions, and extensive anvils have already formed. This sampling discrepancy would naturally

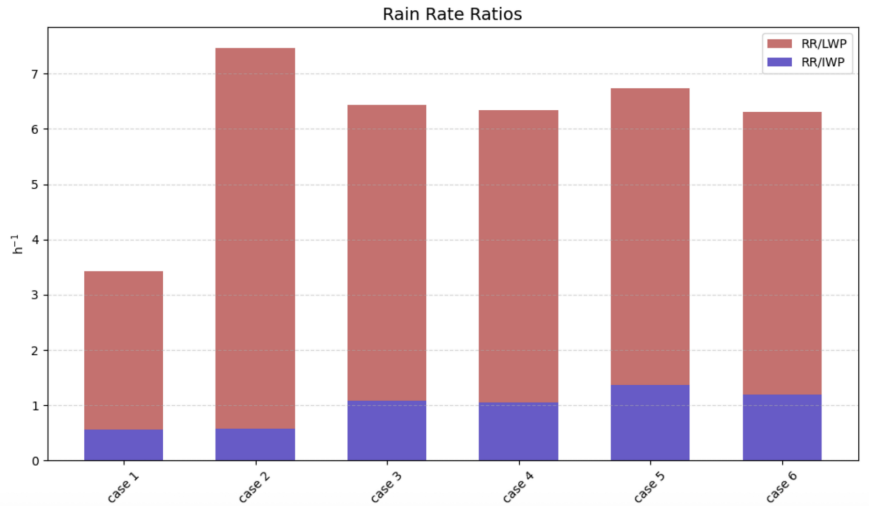

Figure 42: Precipitation efficiency broken up into rain efficiency (RR/LWP) in red and ice efficiency (RR/IWP) in blue, averaged over each case box

lead to the appearance of weaker, less organized systems in the Argentina composite, even though the region is climatologically known for producing some of the deepest and most intense convective systems globally.

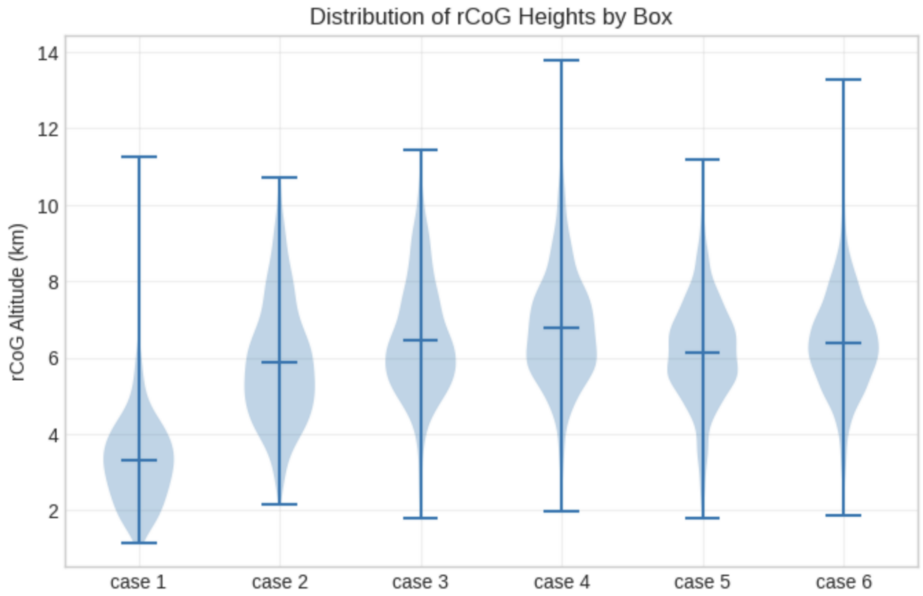

Figure 43: Distributions in rCoG altitude associated with each case box.

Additional insight into these differences emerges from the distribution of rCoG heights shown in Figure 5. The rCoG serves as a proxy for the vertical extent and maturity of the convective core, where higher rCoG values typically correspond to deeper, more vigorous convection with stronger updrafts (Zipser 2003; Houze 2004). In our results, Case 2 (Great Plains) exhibits rCoG heights that are substantially higher than those of the tropical cases, while Case 1 (Argentina) displays markedly lower values. This pattern is unexpected, given that subtropical South America routinely hosts some of the deepest and most intense convection globally (Rasmussen and Houze 2011). The relatively shallow rCoG distribution in Case 1 therefore suggests that many storms within this region were sampled during earlier stages of their lifecycle, prior to the full development of strong, vertically extensive updrafts (e.g., Steiner et al. 1995; Rowe and Houze 2014). Convection at these earlier stages naturally exhibits weaker vertical motion, reduced glaciation aloft, and smaller values of RR, LWP, and IWP, all of which consistent with the lower PE components observed. Conversely, the Great Plains cases appear to reflect storms captured at more mature stages, with stronger and more elevated convective cores, yielding structural characteristics that more closely resemble tropical convection despite their midlatitude location.

These results also suggest a potential broader role of convective lifecycle in shaping precipitation efficiency. Although lifecycle stage was not an explicit focus of the present study, the rCoG distributions and their correspondence to PE components indicate that the timing of storm sampling may influence PE diagnostics. It is plausible that mature convection, with well-developed updrafts and extensive mixed-phase microphysics, could achieve higher efficiencies due, in part, to enhanced riming, aggregation, and condensate fallout (Brdar and Seifert 2018). In contrast, early-stage convection may yield artificially low PE values simply because microphysical pathways have not yet fully developed (Zhang et al. 2022). This emergent sensitivity underscores the importance of considering lifecycle effects in future satellite-based PE assessments, particularly when comparing across regions where convective organization and evolution differ substantially. Incorporating lifecycle classification into subsequent analyses, whether through geostationary tracking (e.g., Jirak et al. 2003; Machado et al. 1998), vertical structure diagnostics, or object-based storm evolution frameworks, would likely refine the interpretation of global PE variability and strengthen the physical consistency of cross-regional comparisons.

4.2 Environmental Influences

Figure 6 provides additional insight into how environmental factors modulate the precipitation efficiency and each component of the PE equation. Several broad patterns emerge across all regions. Most notably, rCoG is strongly and positively correlated with IWP in every case. This relationship is physically intuitive: deeper convection with stronger updrafts lofts more condensate into the upper troposphere, promoting glaciation and increasing the ice water path. Similarly, anvil fraction is consistently and strongly negatively correlated with LWP. Because anvil fraction represents the area of detrained, non-precipitating stratiform cloud relative to the total convective object, a larger anvil footprint corresponds to enhanced ice-dominated cloud area. As more condensate resides in the anvil as ice, less liquid remains available in the lower and middle troposphere, producing lower LWP values. These two relationships, rCoG with IWP and anvil fraction with LWP, behave as expected and appear robust across Cases 1 and 3–6, with only magnitudes varying.

Case 2 (Great Plains), however, departs notably from these regional patterns. Several correlations not only differ in magnitude but actually reverse in sign. The most striking example is the relationship between rCoG and PE. In nearly all other regions, PE and rCoG exhibit a weak to moderate negative correlation, consistent with the idea that stronger updrafts loft more condensate aloft, retaining more ice within the cloud and reducing the fraction that ultimately precipitates out. In Case 2, the correlation is strongly positive. This implying that deeper or more vigorous convection in the Great Plains leads to higher PE, opposite the behavior seen elsewhere. The reason for this reversal becomes clearer when examining Case 2's relationships with environmental shear, moisture, and microphysical structure, all of which diverge from the typical patterns observed in the other cases.

A particularly prominent distinction in Case 2 is the role of vertical wind shear. Across most regions, lower-, mid-, and upper-level shear display only weak and often negligible correlations with any PE component. In Case 2, however, shear emerges as a meaningful and dynamically relevant influence. Midlevel shear is strongly and positively correlated with LWP, and all shear layers show a noticeable negative relationship with PE, being opposite in sign and stronger in magnitude compared to the weak, slightly positive correlations seen in the other regions. This combination suggests that shear in the Great Plains modulates storm structure in a way that retains liquid water aloft while simultaneously suppressing the efficiency with which

hydrometeors reach the surface.

Several physical mechanisms may contribute to this behavior. Enhanced shear can tilt updrafts, allowing developing raindrops to fall into drier air on the storm's downstream side, where they are more likely to evaporate. Strong shear can also support more robust cold pools and downdrafts, which reduce the moisture available to subsequent updrafts and inhibit efficient warm-rain production. Additionally, shear-induced entrainment can introduce dry environmental air into the storm, further increasing evaporation and suppressing precipitation efficiency. Taken together, these processes naturally lead to higher LWP, as condensate is retained aloft for longer periods, and lower PE, as a smaller fraction of that condensate ultimately precipitates. Case 2's unique correlation structure therefore points to a shear-regulated convective regime, in contrast to the more thermodynamically controlled, or underdeveloped, systems in the other regions.

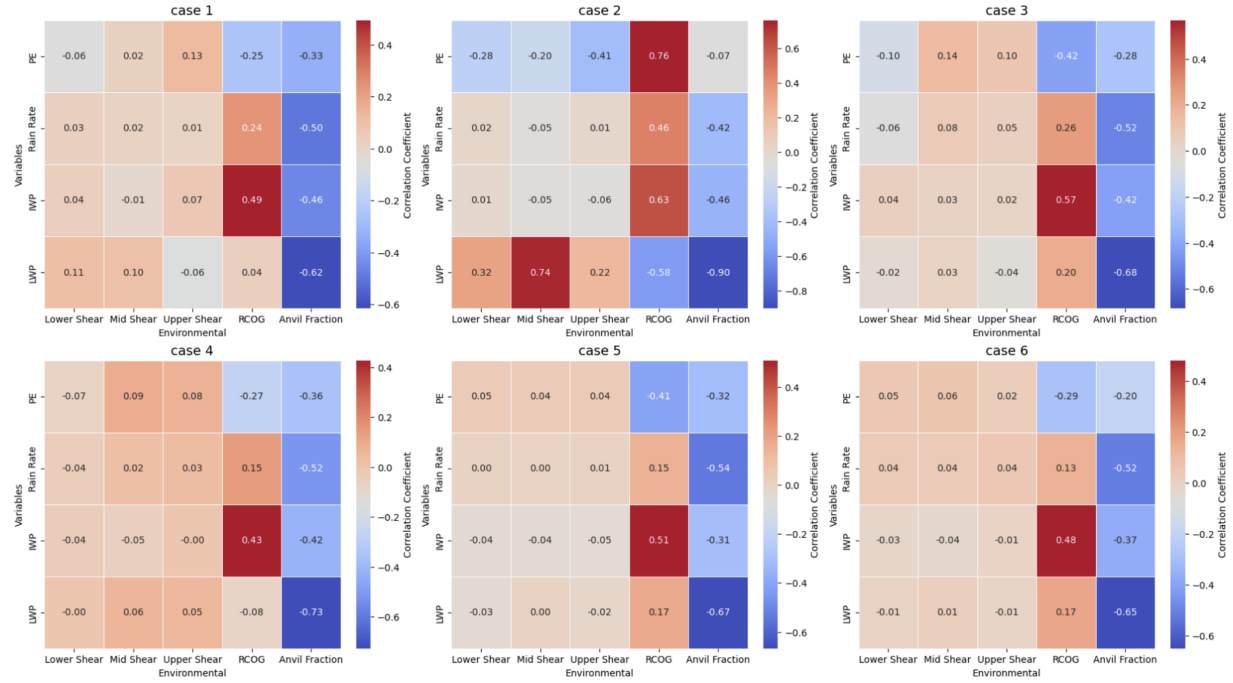

Figure 44: Averaged correlation boxes across each regional box associated with each case. Precipitation efficiency related variables on the y axis, environmental variables on the x axis.

Taken together, these results show that Case 2 (Great Plains) diverges from the other regions because it

occupies a distinct dynamical and environmental regime that strongly influences its precipitation efficiency. Unlike Case 1 (Argentina), where the relatively low rCoG heights point to many systems being sampled early in their lifecycle, before deep updrafts fully develop, the Great Plains cases appear to have been observed during more mature stages, consistent with their exceptionally high rCoG values and enhanced ice lofting. This lifecycle contrast alone can account for much of the difference in condensate partitioning, PE component ratios, and even correlation sign reversals. Meanwhile, the tropical cases (3–6) display remarkable internal consistency: despite spanning both oceanic and coastal environments, they cluster tightly in their PE behavior, vertical structure, and environmental relationships, reflecting the characteristic deep, warm, and weakly sheared convective environment of the equatorial tropics. Case 2 stands apart because it combines strong midlatitude shear, mature deep convection, and substantial ice loading, all conditions that amplify the sensitivity of PE to both dynamical forcing and microphysical pathways. In this context, the Great Plains behaves neither like the early-stage convection in Argentina nor like the deep, thermodynamically driven tropical convection, but instead reflects a unique intersection of lifecycle stage and environmental structure.

4.3 Precipitation Efficiency and Cloud Radiative Properties

Figure 7 illustrates the relationship between anvil fraction and PE, expanding upon the correlations first introduced in Figure 6. As expected, all regions show a decrease in PE with increasing anvil fraction, consistent with the idea that extensive anvils indicate strong ice lofting, reduced liquid water availability, and consequently lower efficiency in converting condensate to precipitation. However, the spread among regions reveals that the sensitivity of PE to changes in anvil fraction is not uniform globally. While more targeted research is needed to quantify these sensitivities, the gradients of the linear regression slopes already provide meaningful physical insight. Notably, despite substantial differences in PE structure, condensate partitioning, and environmental controls between the midlatitude and tropical regions, there is no clear latitude-dependent sensitivity in the anvil–PE relationship. Instead, the most striking contrast emerges within the tropics, specifically between Cases 5 and 6, which correspond to the ascending and descending branches of the Walker Circulation during El Niño conditions.

The ascending branch (Case 5) exhibits the strongest sensitivity of PE to anvil fraction across all cases. This region is characterized by persistent deep convection, vigorous large-scale ascent, and high-column hu-

midity, all of which are conditions that promote substantial anvil generation but also create an environment where additional increases in anvil area strongly limit the availability of liquid water and suppress PE. In contrast, Case 6, representing the descending branch, displays one of the weakest sensitivities. Subsidence-dominated environments typically inhibit deep convection, reduce upper-level moisture, and limit anvil longevity, meaning that increases in anvil fraction exert a far smaller influence on the already low PE characteristic of suppressed convection. This sharp contrast between the ascending and descending Walker branches underscores the influence of large-scale tropical circulations on microphysical pathways and precipitation efficiency. It also raises broader questions about how changes in the Walker Circulation, whether driven by ENSO variability or long-term climate trends, may modulate global patterns of precipitation efficiency through their control of convective depth, humidity structure, and anvil production.

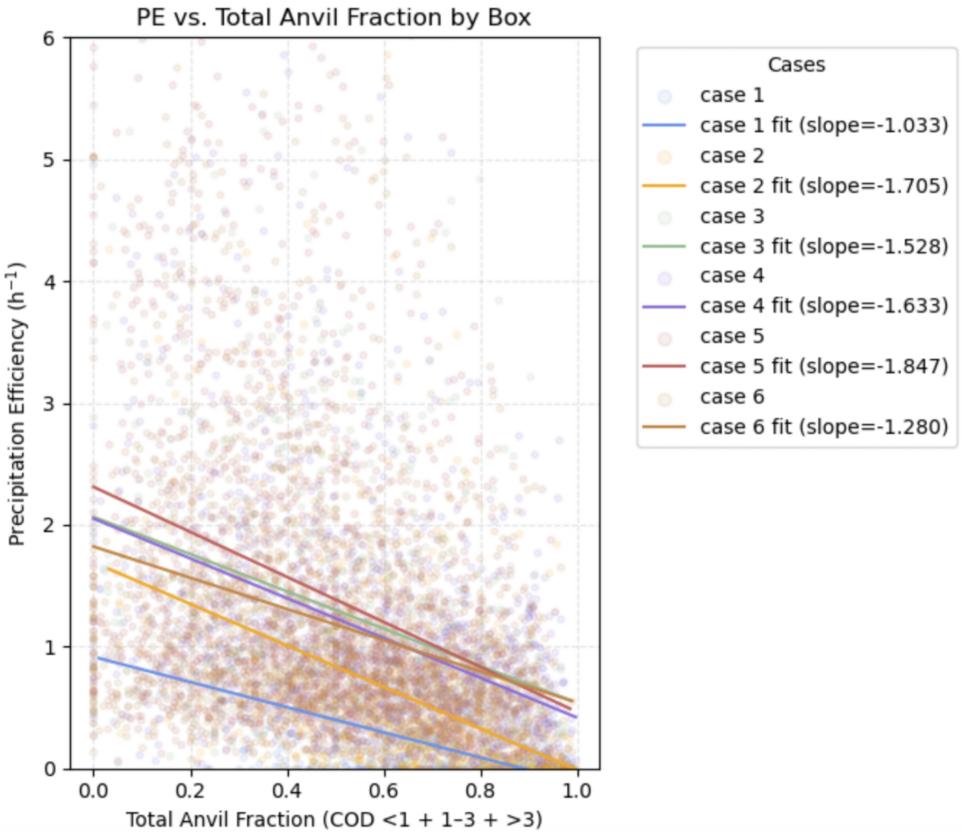

Figure 45: Linear regression demonstrating the relationship between precipitation efficiency and total anvil fraction for each case box.

5 Discussion and Conclusions

Deep convection widely occurs in different weather systems from hurricanes to mesoscale convective systems, to just single cells. Due to the variety of environmental conditions convective objects take place in, it is challenging to find conclusive microphysical properties for all types of events. Furthermore, things such as land versus ocean, and tropical versus midlatitude, provide even more complexity to this topic. While this research attempted to be as comprehensive as possible, land versus ocean considerations, or lack thereof, are a significant limitation of this analysis. This is due to hydrometeor diameter being found to be larger over land than over ocean, thus creating strong implications for available moisture and subsequently impacting ice crystals in convective anvils. This is consistent with stronger updrafts in continental convection (Heymsfield et al. 2010), which showed the maximum updrafts of continental convection are stronger than oceanic convection above 10 km. This is relevant to the ice properties aloft, considering 10 km is approximately where the homogeneous nucleation zone occurs in deep convection, and neglecting maritime and continental influences in this analysis could influence the conclusions of this research.

Although there have been attempts to fix the problem of convective parameterization, the current solutions tend to be more simplistic than what can be seen in reality, which in turn could change convective strength and ice particle properties within a given climate model. In a warming climate, mis-parameterization could be less useful for simulating radiative cloud feedback (Elsaesser et al. 2017), a major motivation for this topic. However, it is believed a lot these issues could be resolved through the further analysis of other regions across the globe using similar methods as presented in this research.

Overall, this analysis demonstrates that precipitation efficiency (PE) varies systematically across storm type, environment, and large-scale dynamical regime, revealing a more complex picture than simple latitudinal distinctions alone can provide. While the midlatitude and tropical cases exhibit clear structural differences, particularly in cloud geometry and hydrometeor loading, these contrasts do not fully explain the observed variability in PE. Instead, metrics of convective vertical structure such as the relative center of gravity (rCoG), together with the local shear environment, emerge as key predictors of regional differences in PE, underscoring the importance of dynamical support and storm maturity. Additionally, PE exhibits a consistent relationship with cloud radiative properties, suggesting that the balance between anvil produc-

tion and surface-reaching precipitation is governed by microphysical pathways that influence both radiative forcing and column water budgets, even if the quantitative magnitude of these links requires further investigation. Finally, the comparison between cases embedded in different phases of the Walker circulation highlights that large-scale vertical motion can exert a stronger influence on PE than latitudinal position, with ascending-regime convection producing markedly different efficiencies than convection forming in subsiding environments. Together, these findings illustrate that PE is shaped by an interplay between storm-scale dynamics, microphysical structure, and planetary-scale circulation patterns, emphasizing the need for future work to consider lifecycle effects and environmental context when interpreting regional or global variations in convective efficiency.

Summary of Key Findings:

- Significant latitudinal differences exist between tropical and midlatitude convective systems.
- The rCoG and vertical shear exhibit region-dependent influences on PE.
- PE demonstrates a relationship with cloud radiative properties, although the precise quantitative extent remains to be determined.
- Large-scale atmospheric circulations contribute to variations in PE, potentially exerting greater influence than latitudinal differences alone.

Future pathways for this work would include additional analysis regarding the role of HIWC and its coincidence to updraft strength, considering this is directly related to the types and abundance of ice crystals seen in the anvils of deep convection. Furthermore, in order to fully address the hydrological implications of precipitation efficiency in a changing climate, this analysis must have a more comprehensive idea of land versus ocean PE differences. Due to the poorer performance of the GMI over land, there would have to be a consideration of more accurate rain rate retrievals, and if ground-based measurements would be more beneficial for an in-depth land analysis. Furthermore, while this paper focused on instances of deep convection, another pathway for future study could be the comparison between shallow and deep convection using these coincidence data sets, or the research of the relationship between PE and convective lifecycle stages, using geostationary satellites. Ultimately these results can be used to improve convective models,

which could allow for better mathematical parameterization, weather forecasting, and understanding the future of the global climate.

References

[1] Anber, Usama M, et al. "Updraft Constraints on Entrainment: Insights from Amazonian Deep Convection." *Journal of the Atmospheric Sciences*, vol. 76, no. 8, 29 May 2019, pp. 2429–2442. https://doi.org/10.1175/jas-d-18-0234.1.

[2] Angulo-Umana, P., & Kim, D. (2023). Mesoscale Convective Clustering Enhances Tropical Precipitation. *Science Advances*, 9(2). https://doi.org/10.1126/sciadv.abo5317

[3] Anip, Mohd Hisham Mohd, and Patrick S. Market. "Dominant Factors Influencing Precipitation Efficiency in a Continental Mid-Latitude Location." *Tellus A: Dynamic Meteorology and Oceanography*, vol. 59, no. 1, 1 Jan. 2007, p. 122. https://doi.org/10.1111/j.1600-0870.2006.00208.x.

[4] Aumann, H. H., & Ruzmaikin, A. (2013). Frequency of Deep Convective Clouds in the Tropical Zone from 10 Years of AIRS Data. *Atmospheric Chemistry and Physics*, 13(21), 10795–10806. https://doi.org/10.5194/acp-13-10795-2013

[5] Biswas, Sounak Kumar, and V. Chandrasekar. "Cross-Validation of Observations between the GPM Dual-Frequency Precipitation Radar and Ground Based Dual-Polarization Radars." *Remote Sensing*, vol. 10, no. 11, 9 Nov. 2018, p. 1773. https://doi.org/10.3390/rs10111773.

[6] Blossey, Peter N., et al. "Cloud-Resolving Model Simulations of KWAJEX: Model Sensitivities and Comparisons with Satellite and Radar Observations." *Journal of the Atmospheric Sciences*, vol. 64, no. 5, 1 May 2007, pp. 1488–1508. https://doi.org/10.1175/jas3982.1.

[7] Bock, L., & Lauer, A. (2024). Cloud Properties and Their Projected Changes in CMIP Models with Low to High Climate Sensitivity. *Atmospheric Chemistry and Physics*, 24(3), 1587–1605. https://doi.org/10.5194/acp-24-1587-2024

[8] Brdar, S., and A. Seifert. "McSnow: A Monte-Carlo Particle Model for Riming and Aggregation of Ice Particles in a Multidimensional Microphysical Phase Space." *Journal of Advances in Modeling Earth Systems*, vol. 10, no. 1, Jan. 2018, pp. 187–206. https://doi.org/10.1002/2017ms001167.

[9] Carbone, Richard E, et al. "Inferences of Predictability Associated with Warm Season Precipitation Episodes." *American Meteorological Society*, vol. 59, no. 13, 1 July 2002, pp. 2033–2056. https://doi.org/10.1175/1520-0469(2002)059¡2033:iopaww¿2.0.co;2.

[10] Chadwick, R., et al. (2015). Large Rainfall Changes Consistently Projected over Substantial Areas of Tropical Land. *Nature Climate Change*, 6(2), 177–181. https://doi.org/10.1038/nclimate2805

[11] Chand, S. S., et al. (2023). Climate Processes and Drivers in the Pacific and Global Warming: A Review for Informing Pacific Planning Agencies. *Climatic Change*, 176(2). https://doi.org/10.1007/s10584-022-03467-z

[12] Chang, Paul S., et al. *Algorithm Theoretical Basis Document: GCOM-W1/AMSR2 Day-1 EDR Compiled by the GCOM-W1/AMSR2 EDR Team. ATBD: GCOM-W1/AMSR2 DAY-1 EDR VERSION 1.0*, 2015.

[13] Dagan, G., & Stier, P. (2020). Constraint on Precipitation Response to Climate Change by Combination of Atmospheric Energy and Water Budgets. *npj Climate and Atmospheric Science*, 3(1). https://doi.org/10.1038/s41612-020-00137-8

[14] Deng, M., et al. (2013). Evaluation of Several A-Train Ice Cloud Retrieval Products with in Situ Measurements Collected during the SPARTICUS Campaign. *Journal of Applied Meteorology and Climatology*, 52(4), 1014–1030. https://doi.org/10.1175/jamc-d-12-054.1

[15] Deng, Min, et al. "CloudSat 2C-ICE Product Update with a New Ze Parameterization in Lidar-Only Region." *Journal of Geophysical Research. Atmospheres*, vol. 120, no. 23, 14 Dec. 2015. https://doi.org/10.1002/2015jd023600.

[16] Djakouré, Sandrine, et al. "Mesoscale Convective Systems and Extreme Precipitation on the West

African Coast Linked to Ocean–Atmosphere Conditions during the Monsoon Period in the Gulf of Guinea." *Atmosphere*, vol. 15, no. 2, 1 Feb. 2024, p. 194. https://doi.org/10.3390/atmos15020194.

[17] Elsaesser, Gregory S, et al. "The Multisensor Advanced Climatology of Liquid Water Path (MAC-LWP)." *Journal of Climate*, vol. 30, no. 24, 1 Dec. 2017, pp. 10193–10210. https://doi.org/10.1175/jcli-d-16-0902.1.

[18] Elsaesser, Gregory S, and Christian D Kummerow. "The Sensitivity of Rainfall Estimation to Error Assumptions in a Bayesian Passive Microwave Retrieval Algorithm." *Journal of Applied Meteorology and Climatology*, vol. 54, no. 2, 1 Feb. 2015, pp. 408–422. https://doi.org/10.1175/jamc-d-14-0105.1.

[19] Elsaesser, Gregory S., et al. "An Improved Convective Ice Parameterization for the NASA GISS Global Climate Model and Impacts on Cloud Ice Simulation." *Journal of Climate*, vol. 30, no. 1, Jan. 2017, pp. 317–336. https://doi.org/10.1175/jcli-d-16-0346.1.

[20] F. Joseph Turk, et al. "Applications of a CloudSat-TRMM and CloudSat-GPM Satellite Coincidence Dataset." *Remote Sensing*, vol. 13, no. 12, 9 June 2021, pp. 2264–2264. https://doi.org/10.3390/rs13122264.

[21] Fankhauser, J C. "Estimates of Thunderstorm Precipitation Efficiency from Field Measurements in CCOPE." *Monthly Weather Review*, vol. 116, no. 3, 1 Mar. 1988, pp. 663–684. https://doi.org/10.1175/1520-0493(1988)116¡0663:eotpef¿2.0.co;2.

[22] Feng, Zhe, et al. "Top-of-Atmosphere Radiation Budget of Convective Core/Stratiform Rain and Anvil Clouds from Deep Convective Systems." *Journal of Geophysical Research Atmospheres*, vol. 116, no. D23, 6 Oct. 2011. https://doi.org/10.1029/2011jd016451.

[23] Gao, Jinyu, et al. "Similarities and Improvements of GPM Dual-Frequency Precipitation Radar (DPR) upon TRMM Precipitation Radar (PR) in Global Precipitation Rate Estimation, Type Classification and Vertical Profiling." *Remote Sensing*, vol. 9, no. 11, 7 Nov. 2017, p. 1142. https://doi.org/10.3390/rs9111142.

[24] Gayet, J.-F., et al. “Microphysical Properties and High Ice Water Content in Continental and Oceanic Mesoscale Convective Systems and Potential Implications for Commercial Aircraft at Flight Altitude.” *Atmospheric Chemistry and Physics*, vol. 14, no. 2, 27 Jan. 2014, pp. 899–912. https://doi.org/10.5194/acp-14-899-2014.

[25] Greenwald, Thomas J, et al. “An Uncertainty Data Set for Passive Microwave Satellite Observations of Warm Cloud Liquid Water Path.” *Journal of Geophysical Research: Atmospheres*, vol. 123, no. 7, 12 Apr. 2018, pp. 3668–3687. https://doi.org/10.1002/2017jd027638.

[26] Hartmann, D. L., & Berry, S. E. (2017). The Balanced Radiative Effect of Tropical Anvil Clouds. *Journal of Geophysical Research: Atmospheres*, 122(9), 5003–5020. https://doi.org/10.1002/2017jd026460

[27] Hartmann, Dennis L, et al. “The Life Cycle and Net Radiative Effect of Tropical Anvil Clouds.” *Journal of Advances in Modeling Earth Systems*, vol. 10, no. 12, 1 Dec. 2018, pp. 3012–3029. https://doi.org/10.1029/2018ms001484.

[28] Hartmann, Dennis L. “Tropical Convection and the Energy Balance at the Top of the Atmosphere.” *American Meteorological Society*, vol. 14, no. 24, 15 Dec. 2001, pp. 4495–4511. https://doi.org/10.1175/1520-0442(2001)014¡4495:tcateb¿2.0.co;2.

[29] Hartmann, Dennis L, and Marc L Michelsen. “No Evidence for Iris.” *Bulletin of the American Meteorological Society*, vol. 83, no. 2, 1 Feb. 2002, pp. 249–254. https://doi.org/10.1175/1520-0477(2002)083¡0249:nefi¿2.3.co;2.

[30] Hartmann, Dennis L., et al. “The Effect of Cloud Type on Earth’s Energy Balance: Global Analysis.” *Journal of Climate*, vol. 5, no. 11, Nov. 1992, pp. 1281–1304. https://doi.org/10.1175/1520-0442(1992)005¡1281:teocto¿2.0.co;2.

[31] Hayden, L., & Liu, C. (2018). A Multiyear Analysis of Global Precipitation Combining CloudSat and GPM Precipitation Retrievals. *Journal of Hydrometeorology*, 19(12), 1935–1952. https://doi.org/10.1175/jhm-d-18-0053.1

[32] Heymsfield, Andrew J., et al. “Microphysics of Maritime Tropical Convective Updrafts at Temperatures from 20° to 60°.” *Journal of the Atmospheric Sciences*, vol. 66, no. 12, 1 Dec. 2009, pp. 3530–3562. https://doi.org/10.1175/2009jas3107.1.

[33] Heymsfield, Gerald M., et al. “Characteristics of Deep Tropical and Subtropical Convection from Nadir-Viewing High-Altitude Airborne Doppler Radar.” *Journal of the Atmospheric Sciences*, vol. 67, no. 2, 1 Feb. 2010, pp. 285–308. https://doi.org/10.1175/2009jas3132.1.

[34] Higgins, Robert, et al. “Influence of the North American Monsoon System on the U.S. Summer Precipitation Regime.” *Journal of Climate*, vol. 10, no. 10, 1 Oct. 1997, pp. 2600–2622. https://doi.org/10.1175/1520-0442(1997)010¡2600:iotnam¿2.0.co;2.

[35] Hong, G., et al. (2009). Parameterization of Shortwave and Longwave Radiative Properties of Ice Clouds for Use in Climate Models. *Journal of Climate*, 22(23), 6287–6312. https://doi.org/10.1175/2009jcli2844.1

[36] Hosking, J. S., et al. “Tropical Convective Transport and the Walker Circulation.” *Atmospheric Chemistry and Physics*, vol. 12, no. 20, 29 Oct. 2012, pp. 9791–9797. https://doi.org/10.5194/acp-12-9791-2012.

[37] Hou, Arthur Y., et al. “The Global Precipitation Measurement Mission.” *Bulletin of the American Meteorological Society*, vol. 95, no. 5, May 2014, pp. 701–722. https://doi.org/10.1175/bams-d-13-00164.1.

[38] Houze, Robert A. “100 Years of Research on Mesoscale Convective Systems.” *Meteorological Monographs*, vol. 59, 1 Jan. 2018, pp. 17.1–17.54. https://doi.org/10.1175/amsmonographs-d-18-0001.1.

[39] Houze, Robert A. “Mesoscale Convective Systems.” *Reviews of Geophysics*, vol. 42, no. 4, 2004. https://doi.org/10.1029/2004rg000150.

[40] Houze, Robert A. “Observed Structure of Mesoscale Convective Systems and Implications for Large-Scale Heating.” *Quarterly Journal of the Royal Meteorological Society*, vol. 115, no. 487, Apr. 1989, pp. 425–461. https://doi.org/10.1002/qj.49711548702.

[41] Hu, Y., and K. Stamnes. "Climate Sensitivity to Cloud Optical Properties." *Tellus B: Chemical and Physical Meteorology*, vol. 52, no. 1, 1 Jan. 2000, p. 81. https://doi.org/10.3402/tellusb.v52i1.16084.

[42] Huaman, Lidia, et al. "Eastward-Propagating Disturbances in the Tropical Pacific." *Monthly Weather Review*, vol. 148, no. 9, 25 Aug. 2020, pp. 3713–3728. https://doi.org/10.1175/mwr-d-20-0029.1.

[43] Huang, Yongjie, et al. "Microphysical Processes Producing High Ice Water Contents (HIWCs) in Tropical Convective Clouds during the HAIC-HIWC Field Campaign: Evaluation of Simulations Using Bulk Microphysical Schemes." *Atmospheric Chemistry and Physics*, vol. 21, no. 9, 6 May 2021, pp. 6919–6944. https://doi.org/10.5194/acp-21-6919-2021.

[44] Huo, J., et al. (2024). A Comparative Study of Cloud Microphysics Schemes in Simulating a Quasi-Linear Convective Thunderstorm Case. *Remote Sensing*, 16(17), 3259. https://doi.org/10.3390/rs16173259

[45] Jing, Xianwen, et al. "A Multimodel Study on Warm Precipitation Biases in Global Models Compared to Satellite Observations." *Journal of Geophysical Research: Atmospheres*, vol. 122, no. 21, 11 Nov. 2017, pp. 11806–11824. https://doi.org/10.1002/2017jd027310.

[46] Jirak, Israel L, et al. "Satellite and Radar Survey of Mesoscale Convective System Development." *Monthly Weather Review*, vol. 131, no. 10, 1 Oct. 2003, pp. 2428–2449. https://doi.org/10.1175/1520-0493(2003)131¡2428:sarsom¿2.0.co;2.

[47] Jo, E., et al. (2025). The Effect of Updraft Entrainment on Convective Cell Deepening in Realistic Large-Eddy Simulations. *Journal of the Atmospheric Sciences*, 82(7), 1361–1379. https://doi.org/10.1175/jas-d-24-0218.1

[48] Kiehl, J. T., et al. "The Simulated Earth Radiation Budget of the National Center for Atmospheric Research Community Climate Model CCM2 and Comparisons with the Earth Radiation Budget Experiment (ERBE)." *Journal of Geophysical Research*, vol. 99, no. D10, 1994, p. 20815. https://doi.org/10.1029/94jd00941.

[49] Korolev, Alexei, et al. "High Ice Water Content in Tropical Mesoscale Convective Systems (a Con-

ceptual Model)." *Atmospheric Chemistry and Physics*, vol. 24, no. 20, 24 Oct. 2024, pp. 11849–11881. https://doi.org/10.5194/acp-24-11849-2024.

[50] Kumjian, Matthew R., et al. "Gargantuan Hail in Argentina." *Bulletin of the American Meteorological Society*, vol. 101, no. 8, 1 Aug. 2020, pp. E1241–E1258. https://doi.org/10.1175/bams-d-19-0012.1.

[51] Kukulies, J., et al. (2021). The Role of Mesoscale Convective Systems in Precipitation in the Tibetan Plateau Region. *Journal of Geophysical Research Atmospheres*, 126(23). https://doi.org/10.1029/2021jd035279

[52] Lebsock, M., & Su, H. (2014). Application of Active Spaceborne Remote Sensing for Understanding Biases between Passive Cloud Water Path Retrievals. *Journal of Geophysical Research: Atmospheres*, 119(14), 8962–8979. https://doi.org/10.1002/2014jd021568

[53] L'Ecuyer, T., et al. (2008). Impact of Clouds on Atmospheric Heating Based on the R04 CloudSat Fluxes and Heating Rates Data Set. *Journal of Geophysical Research*, 113(D8). https://doi.org/10.1029/2008jd009951

[54] L'Ecuyer, Tristan S., et al. "Reassessing the Effect of Cloud Type on Earth's Energy Balance in the Age of Active Spaceborne Observations. Part I: Top of Atmosphere and Surface." *Journal of Climate*, vol. 32, no. 19, 26 Aug. 2019, pp. 6197–6217. https://doi.org/10.1175/jcli-d-18-0753.1.

[55] Lin, Bing, et al. "The Iris Hypothesis: A Negative or Positive Cloud Feedback?" *Journal of Climate*, vol. 15, no. 1, 1 Jan. 2002, pp. 3–7. https://doi.org/10.1175/1520-0442(2002)015¡0003:TIHANO¿2.0.CO;2.

[56] Lin, Lin, et al. "Improved Convective Ice Microphysics Parameterization in the NCAR CAM Model." *Journal of Geophysical Research Atmospheres*, vol. 126, no. 9, 15 Apr. 2021. https://doi.org/10.1029/2020jd034157.

[57] Lindzen, Richard S., et al. "Does the Earth Have an Adaptive Infrared Iris?" *Bulletin of the American Meteorological Society*, vol. 82, no. 3, Mar. 2001, pp. 417–432. https://doi.org/10.1175/1520-0477(2001)082¡0417:dtehaa¿2.3.co;2.

[58] Liu, D., et al. (2015). Underestimation of Oceanic Warm Cloud Occurrences by the Cloud Profiling Radar Aboard CloudSat. *Journal of Meteorological Research*, 29(4), 576–593. https://doi.org/10.1007/s13351-015-5027-5

[59] Liu, Z., et al. (2020). NASA Global Satellite and Model Data Products and Services for Tropical Meteorology and Climatology. *Remote Sensing*, 12(17), 2821. https://doi.org/10.3390/rs12172821

[60] Luiz, et al. "Life Cycle Variations of Mesoscale Convective Systems over the Americas." *American Meteorological Society*, vol. 126, no. 6, 1 June 1998, pp. 1630–1654. https://doi.org/10.1175/1520-0493(1998)126¡1630:lcvomc¿2.0.co;2.

[61] Luke, Edward P, et al. "New Insights into Ice Multiplication Using Remote-Sensing Observations of Slightly Supercooled Mixed-Phase Clouds in the Arctic." *Proceedings of the National Academy of Sciences*, vol. 118, no. 13, 22 Mar. 2021. https://doi.org/10.1073/pnas.2021387118.

[62] Matsui, T., et al. (2016). On the Land–Ocean Contrast of Tropical Convection and Microphysics Statistics Derived from TRMM Satellite Signals and Global Storm-Resolving Models. *Journal of Hydrometeorology*, 17(5), 1425–1445. https://doi.org/10.1175/jhm-d-15-0111.1

[63] Mpheshea, L. E., et al. (2025). The Influence of ENSO-Type on Rainfall Characteristics over Southern Africa during the Austral Summer. *Climate Dynamics*, 63(3). https://doi.org/10.1007/s00382-024-07489-4

[64] Narsey, Sugata, et al. "Convective Precipitation Efficiency Observed in the Tropics." *Geophysical Research Letters*, vol. 46, no. 22, 27 Nov. 2019, pp. 13574–13583. https://doi.org/10.1029/2019gl085031.

[65] Neale, Richard, and Julia Slingo. "The Maritime Continent and Its Role in the Global Climate: A GCM Study." *Journal of Climate*, vol. 16, no. 5, Mar. 2003, pp. 834–848. https://doi.org/10.1175/1520-0442(2003)016¡0834:tmcair¿2.0.co;2.

[66] Nesbitt, Stephen W, et al. "A Census of Precipitation Features in the Tropics Using TRMM: Radar, Ice Scattering, and Lightning Observations." *Journal of Climate*, vol. 13, no. 23, 1 Dec. 2000, pp. 4087–4106. https://doi.org/10.1175/1520-0442(2000)013¡4087:acopfi¿2.0.co;2.

[67] Pilewskie, Juliet, and Tristan L'Ecuyer. "The Role of Convective Intensity in Modulating the Earth's Radiative Balance." *Journal of Climate*, 27 Mar. 2025. https://doi.org/10.1175/jcli-d-24-0334.1.

[68] Power, Scott B., and Ian N. Smith. "Weakening of the Walker Circulation and Apparent Dominance of El Niño Both Reach Record Levels, but Has ENSO Really Changed?" *Geophysical Research Letters*, vol. 34, no. 18, 20 Sept. 2007. https://doi.org/10.1029/2007gl030854.

[69] Qian, Jian-Hua, et al. "Interactions among ENSO, the Monsoon, and Diurnal Cycle in Rainfall Variability over Java, Indonesia." *Journal of the Atmospheric Sciences*, vol. 67, no. 11, 1 Nov. 2010, pp. 3509–3524. https://doi.org/10.1175/2010jas3348.1.

[70] RAMAGE, C. S. "ROLE of a TROPICAL "MARITIME CONTINENT" in the ATMOSPHERIC CIRCULATION1." *Monthly Weather Review*, vol. 96, no. 6, June 1968, pp. 365–370. https://doi.org/10.1175/1520-0493(1968)096¡0365:roatmc¿2.0.co;2.

[71] Rasmussen, Kristen L, and Robert A Houze. "Orogenic Convection in Subtropical South America as Seen by the TRMM Satellite." *American Meteorological Society*, vol. 139, no. 8, 1 Aug. 2011, pp. 2399–2420. https://doi.org/10.1175/mwr-d-10-05006.1.

[72] Rasmussen, Kristen L., et al. "Severe Convection and Lightning in Subtropical South America." *Geophysical Research Letters*, vol. 41, no. 20, 28 Oct. 2014, pp. 7359–7366. https://doi.org/10.1002/2014gl061767.

[73] Robert, Anne, and Houze. "Cloud Clusters and Large-Scale Vertical Motions in the Tropics." vol. 60, no. 1, 1 Jan. 1982, pp. 396–410. https://doi.org/10.2151/jmsj1965.60.1$_3$96.

[74] Roca, R., & Fiolleau, T. (2020). Extreme Precipitation in the Tropics Is Closely Associated with Long-Lived Convective Systems. 1(1). https://doi.org/10.1038/s43247-020-00015-4

[75] Romatschke, Ulrike, and Robert A. Houze. "Extreme Summer Convection in South America." *Journal of Climate*, vol. 23, no. 14, 15 July 2010, pp. 3761–3791. https://doi.org/10.1175/2010jcli3465.1.

[76] Rosenfeld, Daniel, and Itamar M Lensky. "Satellite–Based Insights into Precipitation Formation Processes in Continental and Maritime Convective Clouds." *Bulletin of the American Me-*

teorological Society, vol. 79, no. 11, 1 Nov. 1998, pp. 2457–2476. https://doi.org/10.1175/1520-0477(1998)079¡2457:sbiipf¿2.0.co;2.

[77] Rowe, Angela K, and Robert A Houze. "Microphysical Characteristics of MJO Convection over the Indian Ocean during DYNAMO." *Journal of Geophysical Research. Atmospheres*, vol. 119, no. 5, 14 Mar. 2014, pp. 2543–2554. https://doi.org/10.1002/2013jd020799.

[78] Satoh, Masaki, et al. "Global Cloud-Resolving Models." *Current Climate Change Reports*, vol. 5, no. 3, 17 May 2019, pp. 172–184. https://doi.org/10.1007/s40641-019-00131-0.

[79] Schiro, K. A., & Neelin, J. D. (2019). Deep Convective Organization, Moisture Vertical Structure, and Convective Transition Using Deep-Inflow Mixing. *Journal of the Atmospheric Sciences*, 76(4), 965–987. https://doi.org/10.1175/jas-d-18-0122.1

[80] Smalley, K. M., & Rapp, A. D. (2021). A-Train Estimates of the Sensitivity of the Cloud-To-Rainwater Ratio to Cloud Size, Relative Humidity, and Aerosols. *Atmospheric Chemistry and Physics*, 21(4), 2765–2779. https://doi.org/10.5194/acp-21-2765-2021

[81] Sokol, A. B., & Hartmann, D. L. (2020). Tropical Anvil Clouds: Radiative Driving toward a Preferred State. *Journal of Geophysical Research: Atmospheres*, 125(21). https://doi.org/10.1029/2020jd033107

[82] Steiner, Matthias, et al. "Climatological Characterization of Three-Dimensional Storm Structure from Operational Radar and Rain Gauge Data." *Journal of Applied Meteorology*, vol. 34, no. 9, 1 Sept. 1995, pp. 1978–2007. https://doi.org/10.1175/1520-0450(1995)034¡1978:ccotds¿2.0.co;2.

[83] Stephens, G. L., et al. (2002). THE CLOUDSAT MISSION and the A-TRAIN. *Bulletin of the American Meteorological Society*, 83(12), 1771–1790. https://doi.org/10.1175/bams-83-12-1771

[84] Stephens, Graeme L, et al. "Dreary State of Precipitation in Global Models." *Journal of Geophysical Research*, vol. 115, no. D24, 27 Dec. 2010. https://doi.org/10.1029/2010jd014532.

[85] Stephens, Graeme L, et al. "The Relevance of the Microphysical and Radiative Properties of Cirrus Clouds to Climate and Climatic Feedback." *American Meteorological Society*, vol. 47, no. 14, 1 July 1990, pp. 1742–1754. https://doi.org/10.1175/1520-0469(1990)047¡1742:trotma¿2.0.co;2.

[86] Sui, Chung-Hsiung, et al. "On the Definition of Precipitation Efficiency." *Journal of the Atmospheric Sciences*, vol. 64, no. 12, 1 Dec. 2007, pp. 4506–4513. https://doi.org/10.1175/2007jas2332.1.

[87] Sui, C.-H., et al. (2020). Precipitation Efficiency and Its Role in Cloud-Radiative Feedbacks to Climate Variability. *Journal of the Meteorological Society of Japan Ser II*, 98(2), 261–282. https://doi.org/10.2151/jmsj.2020-024

[88] Sun, De-Zheng, and Richard S Lindzen. "Distribution of Tropical Tropospheric Water Vapor." *Journal of the Atmospheric Sciences*, vol. 50, no. 12, 1 June 1993, pp. 1643–1660. https://doi.org/10.1175/1520-0469(1993)050¡1643:dottwv¿2.0.co;2.

[89] Tao, Wei-Kuo, et al. "The Atmospheric Energy Budget and Large-Scale Precipitation Efficiency of Convective Systems during TOGA COARE, GATE, SCSMEX, and ARM: Cloud-Resolving Model Simulations." *Journal of the Atmospheric Sciences*, vol. 61, no. 20, 1 Oct. 2004, pp. 2405–2423. https://doi.org/10.1175/1520-0469(2004)061¡2405:taebal¿2.0.co;2.

[90] Tian, B. (2005). Diurnal Cycle of Summertime Deep Convection over North America: A Satellite Perspective. *Journal of Geophysical Research*, 110(D8). https://doi.org/10.1029/2004jd005275

[91] Turk, F. Joseph, et al. "Adapting Passive Microwave-Based Precipitation Algorithms to Variable Microwave Land Surface Emissivity to Improve Precipitation Estimation from the GPM Constellation." *Journal of Hydrometeorology*, 29 Apr. 2021. https://doi.org/10.1175/jhm-d-20-0296.1.

[92] Varble, Adam, et al. "Evaluation of Cloud-Resolving and Limited Area Model Intercomparison Simulations Using TWP-ICE Observations: 1. Deep Convective Updraft Properties." *Journal of Geophysical Research Atmospheres*, vol. 119, no. 24, 18 Dec. 2014. https://doi.org/10.1002/2013jd021371.

[93] Vizy, Edward K., and Kerry H. Cook. "Mesoscale Convective Systems and Nocturnal Rainfall over the West African Sahel: Role of the Inter-Tropical Front." *Climate Dynamics*, vol. 50, no. 1–2, 18 Mar. 2017, pp. 587–614. https://doi.org/10.1007/s00382-017-3628-7.

[94] Wane, D., et al. (2023). Atmospheric Response to Seasonal Changes in Sea Surface Tempera-

ture during the Boreal Summer in the Tropical Atlantic. *Climate Dynamics*, 62(3), 1597–1612. https://doi.org/10.1007/s00382-023-06968-4

[95] Wang, Y., et al. (2025). Challenges in Global Climate Models to Represent Cloud Response to Aerosols: Insights from Volcanic Eruptions. *Nature Communications*, 18 Dec. 2025. https://doi.org/10.1038/s41467-025-67359-3

[96] Wolf, K., et al. (2023). Sensitivity of Cirrus and Contrail Radiative Effect on Cloud Microphysical and Environmental Parameters. *Atmospheric Chemistry and Physics*, 23(21), 14003–14037. https://doi.org/10.5194/acp-23-14003-2023

[97] Wu, Shun-Nan, et al. "The Contribution of Mesoscale Convective Systems to the Coastal Rainfall Maximum over West Africa." *Monthly Weather Review*, vol. 152, no. 8, Aug. 2024, pp. 1787–1802. https://doi.org/10.1175/mwr-d-23-0148.1.

[98] Xu, K.-M., et al. (2025). Comparison of Cloud-Type Properties and Radiative Effect Decomposition in Tropical Convectively Active Regions Using CERES High-Resolution Data. *Journal of Geophysical Research: Atmospheres*, 130(19). https://doi.org/10.1029/2025jd043853

[99] Yan, Y., et al. (2021). Effects of Cloud Microphysics on the Vertical Structures of Cloud Radiative Effects over the Tibetan Plateau and the Arctic. *Remote Sensing*, 13(14), 2651. https://doi.org/10.3390/rs13142651

[100] Yang, Gui-Ying, and Julia Slingo. "The Diurnal Cycle in the Tropics." *Monthly Weather Review*, vol. 129, no. 4, Apr. 2001, pp. 784–801. https://doi.org/10.1175/1520-0493(2001)129¡0784:tdcitt¿2.0.co;2.

[101] Yi, B., et al. (2017). A Comparison of Aqua MODIS Ice and Liquid Water Cloud Physical and Optical Properties between Collection 6 and Collection 5.1: Cloud Radiative Effects. *Journal of Geophysical Research Atmospheres*, 122(8), 4550–4564. https://doi.org/10.1002/2016jd025654

[102] Yi, Bingqi. "Diverse Cloud Radiative Effects and Global Surface Temperature Simulations Induced by Different Ice Cloud Optical Property Parameterizations." *Scientific Reports*, vol. 12, no. 1, 22 June 2022. https://doi.org/10.1038/s41598-022-14608-w.

[103] Yun, Kyung-Sook, et al. “Synchronized Spatial Shifts of Hadley and Walker Circulations.” *Earth System Dynamics*, vol. 12, no. 1, 2 Feb. 2021, pp. 121–132. https://doi.org/10.5194/esd-12-121-2021.

[104] Yuan, Jian, and Robert A. Houze. “Global Variability of Mesoscale Convective System Anvil Structure from A-Train Satellite Data.” *Journal of Climate*, vol. 23, no. 21, Nov. 2010, pp. 5864–5888. https://doi.org/10.1175/2010jcli3671.1.

[105] Zeng, Xiping, et al. “An Indirect Effect of Ice Nuclei on Atmospheric Radiation.” *Journal of the Atmospheric Sciences*, vol. 66, no. 1, 1 Jan. 2009, pp. 41–61. https://doi.org/10.1175/2008jas2778.1.

[106] Zhang, Aoqi, et al. “Resilient Dataset of Rain Clusters with Life Cycle Evolution during April to June 2016–2020 over Eastern Asia Based on Observations from the GPM DPR and Himawari-8 AHI.” *Earth System Science Data*, vol. 14, no. 3, 1 Apr. 2022, pp. 1433–1445. https://doi.org/10.5194/essd-14-1433-2022.

[107] Zhao, X., & Liu, X. (2022). Primary and Secondary Ice Production: Interactions and Their Relative Importance. *Atmospheric Chemistry and Physics*, 22(4), 2585–2600. https://doi.org/10.5194/acp-22-2585-2022

[108] Zhao, Pengguo, et al. “Potential Modulation of Aerosol on Precipitation Efficiency in Southwest China.” *Remote Sensing*, vol. 16, no. 8, 18 Apr. 2024, pp. 1445–1445. https://doi.org/10.3390/rs16081445.

[109] Zhou, Y., et al. (2016). Global Parameterization and Validation of a Two-Leaf Light Use Efficiency Model for Predicting Gross Primary Production across FLUXNET Sites. *AGU*, 121(4), 1045–1072. https://doi.org/10.1002/2014jg002876

[110] Zipser, Edward J. “Some Views on “Hot Towers” after 50 Years of Tropical Field Programs and Two Years of TRMM Data.” *Meteorological Monographs*, vol. 29, no. 51, Jan. 2003, pp. 49–49. https://doi.org/10.1175/0065-9401(2003)029¡0049:csvoht¿2.0.co;2.